

Astrocyte-derived clusterin disrupts glial physiology to obstruct remyelination in mouse models of demyelinating diseases

Received: 20 November 2023

Accepted: 26 August 2024

Published online: 06 September 2024

 Check for updates

Chen Chen^{1,2,10}, Yaqing Shu^{1,10}, Chengkai Yan^{1,10}, Huilu Li¹, Zhenchao Huang², ShiShi Shen¹, Chunxin Liu³, Yanjun Jiang^{4,5,6}, Shixiong Huang⁷, Zhanhang Wang⁸, Feng Mei⁹, Feng Qin²✉, Xiaodong Liu^{4,5,6}✉ & Wei Qiu¹✉

Multiple sclerosis (MS) is a debilitating demyelinating disease characterized by remyelination failure attributed to inadequate oligodendrocyte precursor cells (OPCs) differentiation and aberrant astrogliosis. A comprehensive cell atlas reanalysis of clinical specimens brings to light heightened clusterin (CLU) expression in a specific astrocyte subtype links to active lesions in MS patients. Our investigation reveals elevated astrocytic CLU levels in both active lesions of patient tissues and female murine MS models. CLU administration stimulates primary astrocyte proliferation while concurrently impeding astrocyte-mediated clearance of myelin debris. Intriguingly, CLU overload directly impedes OPC differentiation and induces OPCs and OLs apoptosis. Mechanistically, CLU suppresses PI3K-AKT signaling in primary OPCs via very low-density lipoprotein receptor. Pharmacological activation of AKT rescues the damage inflicted by excess CLU on OPCs and ameliorates demyelination in the corpus callosum. Furthermore, conditional knockout of CLU emerges as a promising intervention, showcasing improved remyelination processes and reduced severity in murine MS models.

Prolonged and severe damage to the white matter tracts, encompassing myelinating oligodendrocytes (OLs) and axons within the central nervous system (CNS), constitutes a primary cause of multiple sclerosis (MS). In demyelinated lesions, differentiating myelin-producing oligodendrocytes (OLs) from oligodendrocyte precursor cells (OPCs) is a critical step in the remyelination process¹. However, chronic demyelinating disorders often experience remyelination failure, partly attributed to glia-derived molecules with conflicting effects on OPC differentiation, leading to continuous impediments in myelin

reconstruction and clinical deterioration¹. While current MS therapies predominantly target immune modulation, their efficacy in promoting remyelination is limited^{2–4}. The intricate interactions among glial cells are increasingly acknowledged as crucial regulators of the oligodendrocyte-intrinsic program governing physiological OL maturation^{5,6}. Despite their potential, the glial mechanisms influencing aberrant OPC differentiation and remyelination failure in the context of MS^{7,8} require further investigation to develop effective pharmacological strategies.

¹Department of Neurology, The Third Affiliated Hospital of Sun Yat-sen University, Guangzhou, China. ²Department of Neurosurgery, Lingnan Hospital, The Third Affiliated Hospital of Sun Yat-sen University, Guangzhou, China. ³Department of Emergency, The Third Affiliated Hospital of Sun Yat-sen University, Guangzhou, China. ⁴Department of Anaesthesia and Intensive Care, Faculty of Medicine, The Chinese University of Hong Kong, Hong Kong SAR, China. ⁵Li Ka Shing Institute of Health Science, The Chinese University of Hong Kong, Hong Kong SAR, China. ⁶Peter Hung Pain Research Institute, The Chinese University of Hong Kong, Hong Kong SAR, China. ⁷Department of Neurology, Hainan General Hospital (Hainan Affiliated Hospital of Hainan Medical University), Haikou, Hainan, China. ⁸Department of Neurology, 999 Brain Hospital, Guangzhou, China. ⁹Department of Histology and Embryology, Third Military Medical University (Army Medical University), Chongqing, China. ¹⁰These authors contributed equally: Chen Chen, Yaqing Shu, Chengkai Yan. ✉e-mail: qinfeng2@mail.sysu.edu.cn; xdliu@cuhk.edu.hk; qiuwei@mail.sysu.edu.cn

Astrocytes, the predominant cell type in the CNS, play vital roles in myelin formation during mammalian development. In response to acute or chronic pathological stimuli, astrocytes undergo reactive changes, influencing factors such as OL survival, neurotoxicity, microglial phenotype, inflammatory cell infiltration, and the immunometabolic landscape in the brain⁸. These reactive astrocytes significantly impact the outcome of neurological disorders, including MS and Alzheimer's disease^{7,9,10}. Previous studies have implicated astrocyte-derived molecules, such as endothelin-1, in inhibiting remyelination¹¹, highlighting the potential influence of reactive astrocytes in demyelinating diseases. Conversely, hypertrophic astrocytes in active MS lesions have been shown to phagocytose myelin debris, indicating a complex role in demyelination and remyelination processes^{12,13}. Inefficient clearance of myelin debris due to astrocyte suppression can impair OPC facilitation and hinder remyelination progress¹⁴.

Clusterin (CLU), also known as Apolipoprotein J, is ubiquitously distributed in mammalian body fluids. The secretory form, sCLU, is a highly glycosylated heterodimer consisting of α/β chains cleaved from the polypeptide. As a molecular chaperone, sCLU plays roles in lipid transport, apoptosis, cell differentiation, debris clearance, and immune modulation^{15,16}. Studies have reported increased expression of CLU in the cerebrospinal fluid (CSF)^{17–19} and peripheral blood of MS patients^{20,21}. Single-cell transcriptomic analyses suggest selective CLU expression in astrocytes, particularly in a subpopulation of astrocytes within active MS lesions⁷. However, the contribution of dysregulated CLU to astrocyte-related pathological activities in demyelinating lesions in MS remains unexplored.

This study delves into the pathogenic role of astrocytic CLU in a murine model of demyelinating lesions. Our findings indicate that autocrine and paracrine CLU suppress astrocytic clearance of myelin debris and OPC differentiation, representing a potential pathological factor contributing to remyelination failure in MS models. This study proposes CLU as a therapeutic target to enhance remyelination in demyelinating diseases.

Results

CLU is upregulated by astrocytes in both MS and experimental demyelinating lesions

Several clinicopathological studies have reported the presence of CLU in demyelinating lesions, CSF, and serum of MS patients, with astrocytes in chronic active lesions identified as the primary source of CLU^{19–25}. A recent comprehensive study utilized single-nucleus RNA sequencing data to delineate the cell atlas and cell-cell communication within patient tissues under various pathological conditions⁷. Re-analyzing this dataset revealed four distinct astrocyte subtypes (termed Ast1–4) with various ratios in different pathological regions (Supplementary Fig. 1A). While CLU is designated as a marker gene for astrocytes (Supplementary Fig. 1B), Ast2 exhibited a higher expression of CLU than other astrocytes, identifying it as an active lesion edge-specific astrocyte subtype (Supplementary Fig. 1C–E), implicating CLU in the active lesions of MS. Our cohort's site- and cell type-specific distribution of CLU protein corroborated these findings. In the MS white matter, astrocyte hypertrophy was evident, with CLU highly expressed in up to 60.7% of GFAP⁺ astrocytes at the active edge (compared to 15.5% in controls, $p < 0.001$, Fig. 1A, B). Importantly, CLU was not co-expressed in IBA1⁺ microglia, PDGFR α ⁺ OPC, CCI⁺ OL, NeuN⁺ neurons, or CD31⁺ vascular endothelial cells in EAE models (Supplementary Fig. 1F), confirming its exclusive expression in astrocytes. We further examined CLU's expression pattern in rodent models of demyelinating diseases. In EAE models, CLU expression dramatically increases following CFA immunization and is co-labeled with GFAP in the spinal cord's white matter (Fig. 1C, D). Moreover, CLU protein levels correlated positively with EAE scores (Fig. 1E, F), suggesting a link between CLU expression and disease progression. Similarly,

significantly increased CLU-positive astrocytes were observed at different time points after immunization in LPC-induced demyelinating disorder models (Fig. 1G, H). Surprisingly, in cuprizone-induced demyelination models, neither CLU upregulation nor increased overlap between GFAP and CLU was detected, as shown in immunofluorescence and western blotting assays (Fig. 1I–L).

Suppression of astrocytic phagocytosis of myelin debris by CLU

To assess the pathological effects of CLU, we investigated its autocrine impact on astrocytes. Bulk RNA sequencing was conducted on primary astrocytes following in vitro CLU treatment for 24 h (Supplementary Fig. 2A). This revealed significant modulation, with 173 upregulated and 301 downregulated differentially expressed genes (DEGs, CLU vs. DPBS, fold change >1.5 or <-1.5 , adjusted $p < 0.05$, Supplementary Fig. 2B and Supplementary Dataset 1). Gene annotation through Metascape²⁶ highlighted enrichment in pathways associated with CLU's known molecular functions annotated in the NCBI Gene database. For instance, terms like “*regulation of signaling receptor activity*” and “*cytokine-cytokine receptor interaction*” (Supplementary Fig. 2C) are pertinent to CLU-related “*enables signaling receptor binding*” in the Gene database. Gene set enrichment analysis (GSEA) employing KEGG gene sets also suggested the potential impacts of CLU on signaling transduction (Supplementary Fig. 2D). Notably, the upregulated DEGs were also enriched for terms related to proliferation and astrocyte differentiation (including “*positive regulation of gliogenesis*”), indicating a role of CLU in gliogenesis. Indeed, CLU administration significantly promoted EdU incorporation into the DNA of primary astrocytes (Supplementary Fig. 2E, F) and increased astrocyte culture cell numbers dose-dependently (Supplementary Fig. 2G). Consistent findings were observed in vivo when an osmotic pump continuously releasing CLU over 7 days was implanted over the corpus callosum, resulting in a significant increase in astrocyte numbers (GFAP⁺/ALDH1L1⁺) compared to the PBS control (Supplementary Fig. 2H, I). These results support the notion that CLU accelerates astrogliosis both in vivo and in vitro.

Given the generation of myelin debris in MS due to recurrent demyelination, we explored CLU's involvement in astrocyte-mediated myelin fragment clearance. Lipocalin 2 (LCN2) is essential for myelin uptake by astrocytes²⁷. After 48 h of treatment, CLU (200 and 400 ng/mL) significantly downregulated LCN2 protein levels in primary astrocytes (Supplementary Fig. 2J, K). Moreover, CLU (200 ng/mL) exposure notably reduced the intracellular overlap of CFSE-labeled myelin debris and lysosome markers (Lysotracker Red) in the myelin phagocytosis assay (Supplementary Fig. 2L, M), a result confirmed by western blot (Supplementary Fig. 2N, O). These findings establish that CLU suppresses astrocytic clearance of myelin debris, implicating it in the pathogenesis of demyelinating diseases.

Considering that microglia also have a myelin phagocytic function and play essential roles in the CNS, we investigated CLU's involvement in microglia-mediated myelin fragment clearance using fluorescent staining and flow cytometry. The results showed that microglia clearance of myelin debris remained unchanged in primary microglia following CLU stimulation (Supplementary Fig. 2P–S).

Transcriptomic alterations in OPCs induced by CLU exposure

To unravel the paracrine effects of CLU, we delved into its impact on OPCs, given the crucial role of insufficient OPC differentiation in impeding remyelination in MS. Recognizing the dynamic cross-talk between reactive astrocytes and OPCs, which contributes to OPC suppression^{8,28,29}, we explored whether astrocyte-derived CLU acts as a mediator in astrocyte-OPC interactions. Employing bulk RNA sequencing, we subjected OPCs, differentiated from primary NPCs, to treatment with DPBS or 200 ng/mL recombinant CLU protein for 3 or 24 h (Fig. 2A).

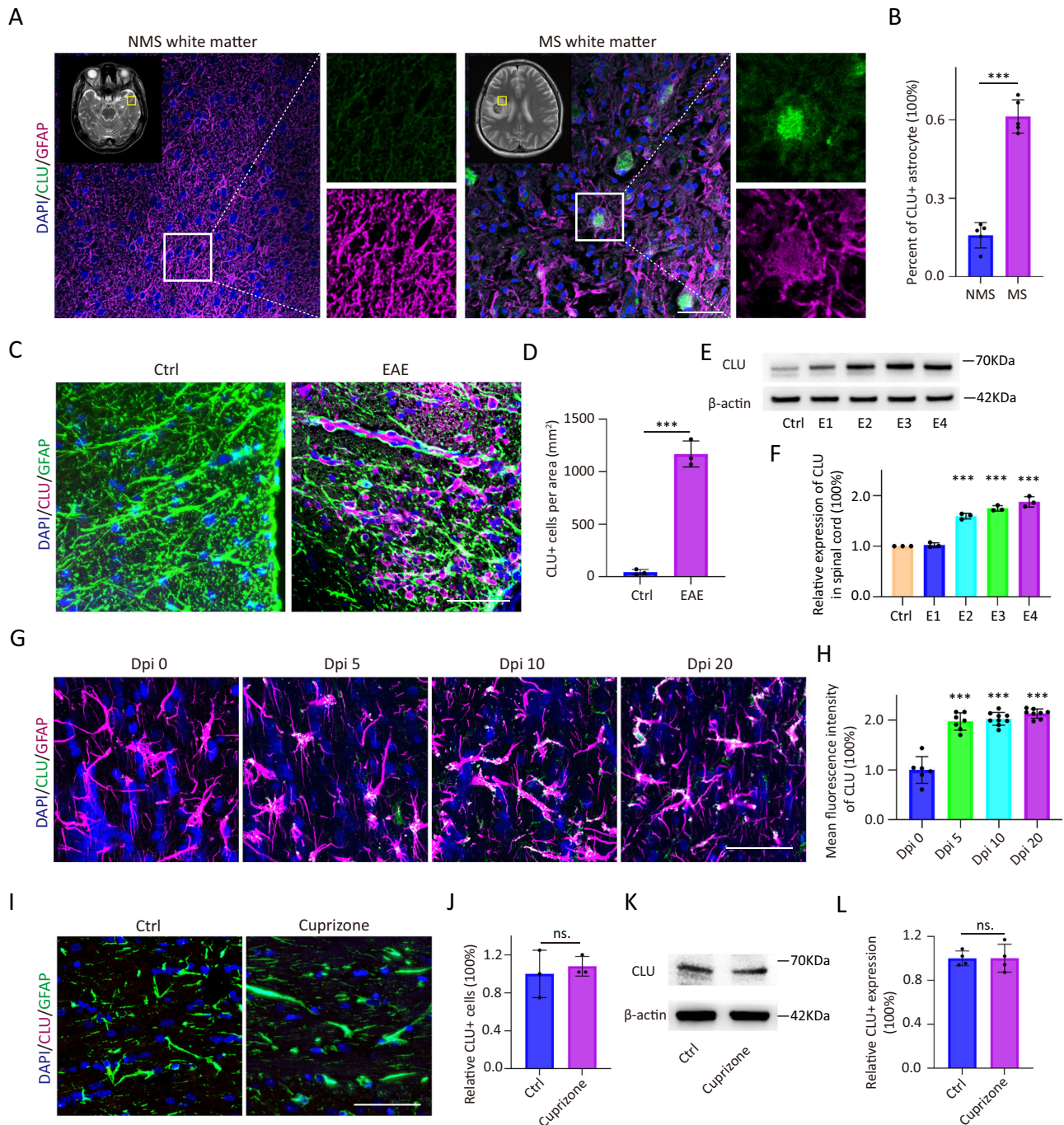


Fig. 1 | CLU is upregulated by astrocytes in MS as well as murine demyelinating lesions. **A, B** Representative micrographs depicting immunohistochemical staining of CLU and GFAP within the white matter lesions of MS and NMS patients ($n = 1$ participant/group, $p < 0.0001$). **C, D** Immunohistochemical staining revealing elevated CLU levels in the astrocyte within the spinal cord of EAE ($n = 3$ mice/group, $p = 0.0001$). **E, F** Western blot analysis demonstrates a progressive increase in CLU levels correlated with disease severity in the spinal cord of EAE mice ($n = 3$ mice/group, E1 vs. Ctrl $p = 0.4528$; E2 vs. Ctrl $p < 0.0001$; E3 vs. Ctrl $p < 0.0001$; E4 vs. Ctrl $p = 0.0001$). **G, H** Increased CLU levels are observed in LPC-induced demyelinated

foci ($n > 5$ mice/group, Dpi 5 vs. dpi 0 $p < 0.0001$, Dpi 10 vs. dpi 0 $p < 0.0001$, Dpi 20 vs. dpi 0 $p < 0.0001$). **I–L** In cuprizone-induced demyelinated foci, CLU levels remain unchanged, as evidenced by immunohistochemical staining ($n = 3$ mice/group, $p = 0.6358$) and western blot ($n = 4$ mice/group, $p = 0.9852$). For immunofluorescence pictures: Scale bar: 50 μm . Statistical analysis was performed using unpaired two-tailed Student's t -tests, mean \pm SD, * $p < 0.05$, ** $p < 0.01$, *** $p < 0.001$. ns. = p not significant. NMS non-multiple sclerosis, MS multiple sclerosis, Ctrl control, EAE experimental autoimmune encephalomyelitis, E clinical score for EAE, LPC lysocleithin.

While minimal gene changes were observed at 3 h of CLU treatment, identifying relatively few genes as DEGs (defined as fold changes between groups >1.5 with $p < 0.05$) (Supplementary Dataset 2), GO annotation in GSEA indicated toxic effects of CLU on OPCs, with enrichment in processes such as “response to toxic

substance” and “mitochondrial outer membrane permeabilization involved in programmed cell death” (Fig. 2B). Additionally, GSEA using KEGG gene sets highlighted the enrichment of various signaling pathways (Supplementary Dataset 3), including the *PI3K-AKT* signaling pathway, which is frequently implicated in OPC

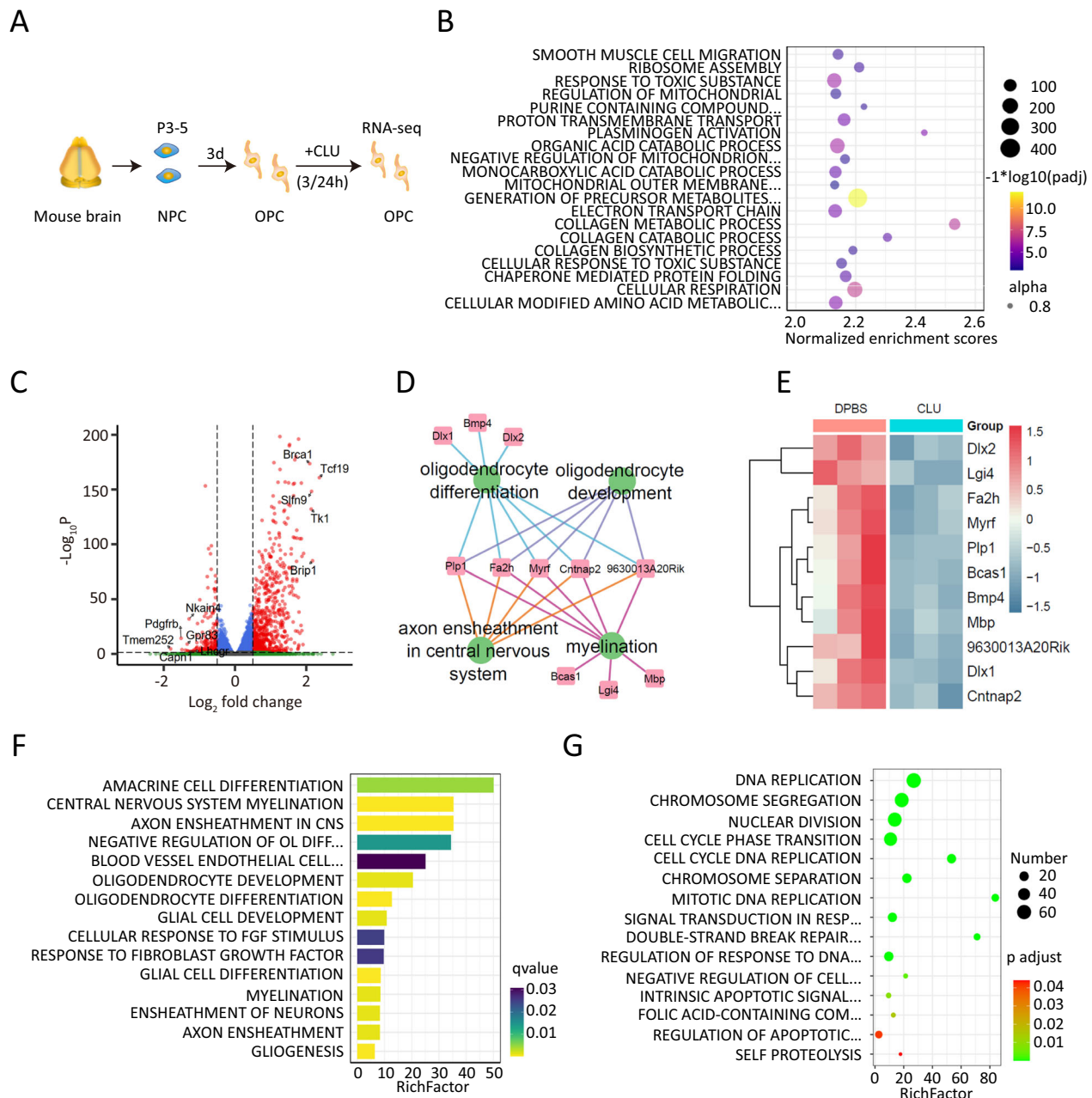


Fig. 2 | Impact of CLU exposure on the transcriptome of OPCs. A Schematic diagram outlining the protocols for RNA sequencing of OPCs treated with CLU. **B** GSEA revealed the toxic effects of CLU on OPCs after 3 h of treatment ($n = 3$ mice/group). **C** Volcano plot displaying DEGs in OPCs treated with CLU for 24 h ($n = 3$ mice/group). **D–F** Gene Ontology annotation using downregulated genes

highlighted the enrichment of biological processes (BPs) relevant to OL differentiation, myelination, and axon ensheathment after 24 h of treatment with CLU at 200 ng/mL ($n = 3$ mice/group). **G** Gene Ontology annotation using upregulated DEGs revealed several GOBPs associated with DNA damage ($n = 3$ mice/group).

differentiation, proliferation, and apoptosis. These findings suggested a potential role of PI3K-AKT signaling pathway inhibition in CLU-mediated destructive effects.

Significant transcriptomic shifts were evident after 24 h of exposure, with 615 upregulated and 189 downregulated DEGs (CLU vs. DPBS, fold change >1.5 or <-1.5 , adjusted $p < 0.05$, Fig. 2C and Supplementary Dataset 4). Downregulated genes were associated with biological processes (BPs) relevant to OL differentiation, myelination, and axon ensheathment (Fig. 2D–F). Conversely, upregulated DEGs were enriched in GOBPs related to DNA replication, DNA damage response, and double-strand break repair (Fig. 2G). Prolonged CLU exposure appeared to induce DNA damage, potentially mediating OPC proliferation inhibition and apoptosis.

CLU overload mediates the loss of OPC and myelin in the corpus callosum

The observed transcriptomic changes were validated through both in vitro and in vivo assessments. OPCs were subjected to varying concentrations (50 ng/mL, 100 ng/mL, 200 ng/mL, and 400 ng/mL) of CLU protein for 5 days in differentiation medium (Fig. 3A). A dose-dependent reduction in MBP⁺ cells was evident, indicating that CLU could directly impede OPC differentiation (Fig. 3B, C). Concurrently, CLU administration at different doses diminished EdU incorporation (Fig. 3D, E) and increased cleaved caspase-3 (CC3, an apoptosis marker) levels in Olig2⁺ cells, as revealed by immunofluorescence (Fig. 3F, G) and western blot analyses (Fig. 3H, I). To evaluate the time-dependent effect of CLU on OPC differentiation, primary OPC cultures

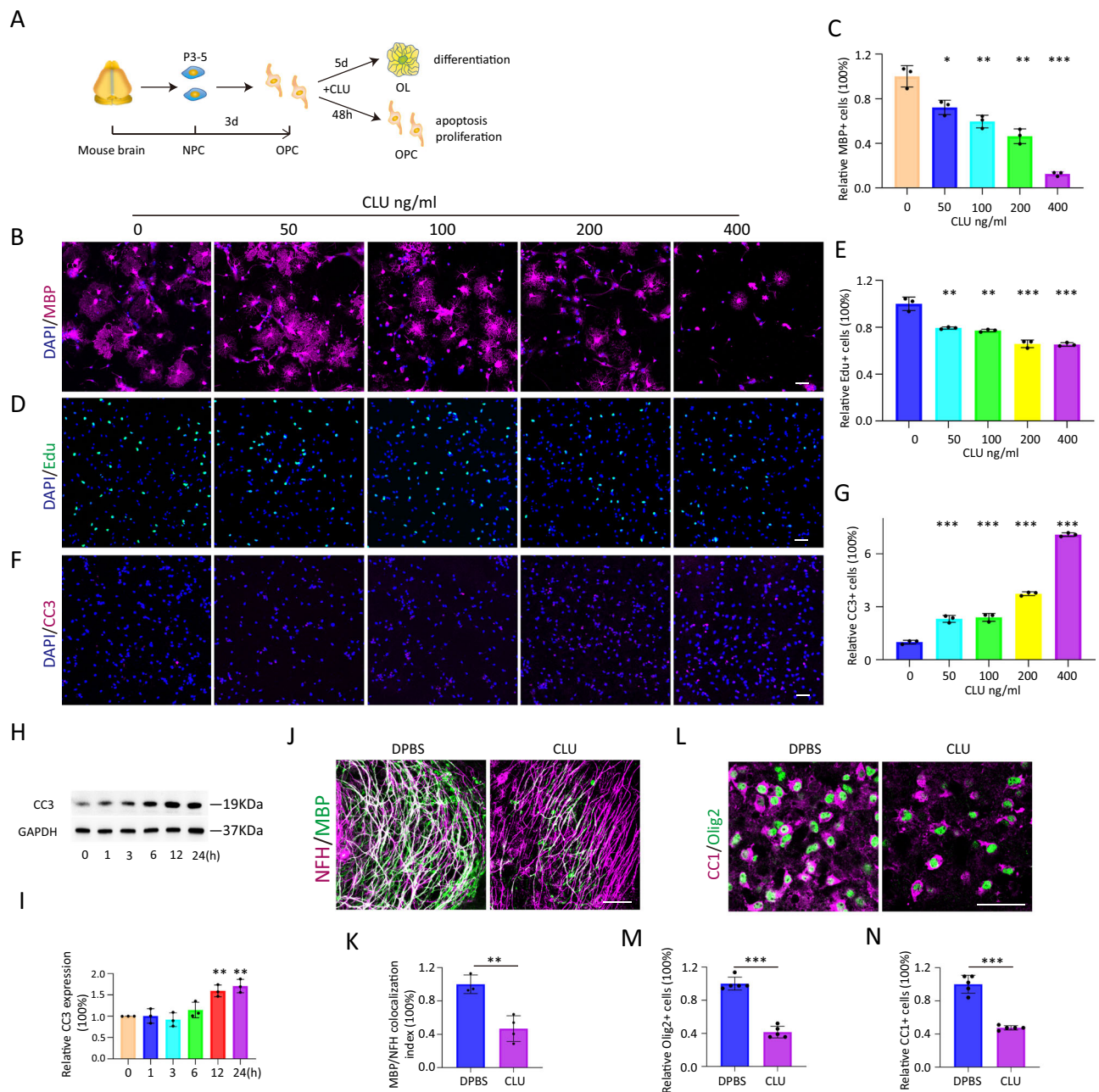


Fig. 3 | Impact of CLU on OPC differentiation and apoptosis in vitro.

A Schematic diagram illustrating OPC differentiation, proliferation, and apoptosis assays treated with CLU. **B, C** CLU exhibited a dose-dependent decrease in the number of MBP⁺ cells in the OPC differentiation assay ($n = 3$ technical replicates/group, 50 ng/mL vs. 0 ng/mL $p = 0.0141$; 100 ng/mL vs. 0 ng/mL $p = 0.0032$; 200 ng/mL vs. 0 ng/mL $p = 0.0013$; 400 ng/mL vs. 0 ng/mL $p = 0.0001$). **D, E** In the OPC proliferation assay, CLU dose-dependently reduced the number of Edu⁺Olig2⁺ cells ($n = 3$ technical replicates/group, 50 ng/mL vs. 0 ng/mL $p = 0.0035$; 100 ng/mL vs. 0 ng/mL $p = 0.0025$; 200 ng/mL vs. 0 ng/mL $p = 0.0008$; 400 ng/mL vs. 0 ng/mL $p = 0.0005$). **F, G** CLU dose-dependently increased OPC apoptosis, as detected by cleaved caspase-3 immunohistochemical staining ($n = 3$ technical replicates/group, 50 ng/mL vs. 0 ng/mL $p = 0.0005$; 100 ng/mL vs. 0 ng/mL $p = 0.0005$; 200 ng/mL

vs. 0 ng/mL $p < 0.0001$; 400 ng/mL vs. 0 ng/mL $p < 0.0001$). **H, I** CLU dose-dependently increased OPC apoptosis, confirmed by CC3 expression via western blot ($n = 3$ technical replicates/group, 1 h vs. 0 h $p = 0.9447$; 3 h vs. 0 h $p = 0.4328$; 6 h vs. 0 h $p = 0.2383$; 12 h vs. 0 h $p = 0.0017$; 24 h vs. 0 h $p = 0.0014$). **J, K** CLU inhibited the ability of OPCs to form a myelin sheath in cerebellar organic slice culture ($n \geq 3$ technical replicates/group, $p = 0.0033$). **L–N** Numbers of Olig2⁺ OPCs and CC1⁺ OLs in the cerebellar slices were reduced after CLU treatment ($n = 5$ technical replicates/group, $p < 0.0001$; $p = 0.0003$). For immunofluorescence pictures: Scale bar: 50 μ m. Statistical analysis was performed using unpaired two-tailed Student's *t*-tests, mean \pm SD, * $p < 0.05$, ** $p < 0.01$, *** $p < 0.001$. ns. = p not significant. CC3 cleaved caspase-3.

were incubated in oligodendrocyte medium for 5 days to allow differentiation. Recombinant CLU protein (200 ng/mL) was added to the cultures immediately, with DPBS used as the control (Supplementary Fig. 3A). As illustrated in Supplementary Fig. 3C, D, the number of MBP-positive cells gradually decreased with CLU exposure, compared to control cultures. To assess the effect of CLU administration on OPC

proliferation and survival over time, primary OPCs were maintained in an OPC medium and treated with 200 ng/mL CLU at different time points, as described above (Supplementary Fig. 3B). CLU treatment time-dependently inhibited Edu incorporation (Supplementary Fig. 3E, F) and increased CC3 levels (Supplementary Fig. 3G, H), indicating that CLU effectively suppressed OPCs proliferation and survival

as early as 24 h after administration. To assess the effect of CLU administration on OLs survival, OPC-induced OLs was cultured in OLs medium and treated with 200 ng/mL CLU at different time points (Supplementary Fig. 3I). The increased CC3 (Supplementary Fig. 3J–M) and reduced MBP (Supplementary Fig. 3N, O) expression were observed, indicated that CLU also could promote OLs apoptosis *in vitro*. These findings highlight that CLU exerts a rapid and direct impact on OPCs and OLs maintenance and differentiation.

Similar outcomes were replicated in the *in vitro* culture of cerebellar organic brain slices treated with 200 ng/mL of CLU. Notably, CLU hindered OPC's ability to form myelin sheaths around axons in the organic slice culture, as indicated by the significant reduction in co-labeled MBP and NFH in cerebellar slices (Fig. 3J, K). Moreover, Olig2⁺ OPCs and CCI⁺ OLs in the cerebellar slices were also reduced (Fig. 3L–N).

To explore CLU's impacts on OPCs, OLs, and myelin *in vivo*, NG2-CreER2 mice were crossed with tau^{mGFP} mice, generating NG2-CreERT2::tau^{mGFP} reporter mice. Cre expression was induced in NG2⁺ OPC (polydendrocytes) by tamoxifen in 8-week-old female mice, leading to mGFP expression marking newly generated myelin over 4 weeks. Afterward, mice were randomly assigned into two groups and administered with either DPBS or CLU into the corpus callosum for 7 days via implantable osmotic pumps (Fig. 4A). Compared to DPBS vehicle control, CLU administration significantly and directly harmed OLs, as demonstrated by the decrease in new myelinated area (mGFP positive) and the length of new myelin in the corpus callosum (Fig. 4B–D). Additionally, lower counts of NG2⁺ OPCs and CCI⁺ OLs were observed following CLU exposure (Supplementary Fig. 4A–C). Myelin proteolipid protein (PLP, a major myelin protein) staining and transmission electron microscopy (TEM) revealed a decrease in myelin sheath thickness in CLU-treated mice, as evidenced by the significantly lower fluorescence intensity of PLP and thinner myelin sheaths in the corpus callosum (Supplementary Fig. 4D, E, F). The diameter of axons was not affected by CLU (Fig. 4G). These findings collectively highlight the damaging effects of CLU on OPCs, OLs, and myelin in the corpus callosum without impacting the axon diameter.

Astrocytic CLU overexpression induces OPCs, OLs and myelin loss in the corpus callosum

In a parallel investigation, the Cre-DIO system was employed to achieve high expression of CLU, specifically in astrocytes. Wild mice were co-injected with rAAV-GfaABCID-Cre-EGFP (AAV-Cre) along with either rAAV-CMV-Dio-mCherry (Dio-NC) or rAAV-CMV-Dio-CLU-mCherry (Dio-CLU) in the corpus callosum (Fig. 4H). After 3 weeks, substantial astrocytes in the corpus callosum were marked by EGFP and mCherry, with CLU upregulated approximately 6-fold in Dio-CLU injected mice compared to Dio-NC injected mice (Supplementary Fig. 4F, G). Six weeks post-AAV infection, CLU overexpression significantly reduced NG2⁺ OPCs and CCI⁺ OLs in the corpus callosum compared to the Dio-NC control (Fig. 4I, J, L, M). In addition, the proportion of CC3⁺ OPCs and CC3⁺ OLs significantly increased in AAV-Cre and Dio-CLU co-injected mice, indicating that the apoptosis of OPCs and OLs was promoted by CLU upregulation in astrocytes (Fig. 4K, N). TEM analysis further revealed a decrease in myelin sheath thickness in AAV-Cre and Dio-CLU co-injected mice compared to the AAV-Cre and Dio-CLU co-injected group (Fig. 4O, P). The CLU-induced percent of unmyelinated axons was confirmed to be increased, while the diameter of the axons was not affected (Fig. 4Q, R).

VLDLR knockdown in OPCs alleviated CLU injury *in vivo*

To consolidate the direct effect of CLU on OPCs, we assessed the expression of CLU receptors in OPCs and performed receptor knockdown to reverse the deleterious effects of CLU. Previous studies have identified ApoER2 and VLDLR as cell membrane receptors for CLU^{30–33}, triggering Reelin-like signaling and activating the PI3K/Akt signal

pathway³⁰. We measured the expression of ApoER2 and VLDLR in NPC-induced OPCs and primary astrocyte lysates, revealing that ApoER2 is primarily expressed in astrocytes while VLDLR is expressed in OPCs (Supplementary Fig. 5A, B). To study the receptor function in CLU-mediated injuries, we examined the expression of VLDLR in OPCs, OLs, and ApoER2 in astrocytes during normal development and after demyelination. The results showed elevated levels of VLDLR in OPCs and OLs, and ApoER2 in astrocytes on the 14th day after birth (p14), gradually decreasing thereafter (Supplementary Fig. 5C–F). In LPC models, VLDLR expression decreased on OPCs at dpi21 and on OLs from dpi5 onwards, with no significant changes in ApoER2 expression on astrocytes at any tested time points (Supplementary Fig. 5G–J). In the EAE model, conducted 15 days after immunization, when mice exhibited peak clinical disease scores, VLDLR expression decreased in OPCs but not OLs compared to the normal control group. Additionally, ApoER2 was slightly upregulated in astrocytes in EAE mice (Supplementary Fig. 5K–N). However, ApoER2 expression in primary astrocytes remained unchanged after CLU stimulation, regardless of concentration or duration of stimulation (Supplementary Fig. 5O–R). Despite changes in CLU receptors, the upregulation of CLU may primarily drive CLU signaling in disease models, as evidenced by the extent of CLU dysregulation and the therapeutic effects of CLU knockdown.

To further assess the direct effect of CLU on OPCs, we engineered lentivirus carrying VLDLR shRNA in a miR30a backbone (shRNAmirs) driven by the NG2-promoter, enabling selective shRNA expression in OPCs (Fig. 5A, B). The lentivirus carrying specific shRNA or scramble control was injected into the corpus callosum on day 0, followed by the implantation of a mini pump containing CLU on day 7. After 7 days of pumping, mice were sacrificed, and brain samples were collected for experiments (Fig. 5C). The results demonstrated that specific knockdown of VLDLR in OPCs alleviated CLU-induced injury, manifested by increased OPCs, Edu⁺ OPCs, and decreased CC3⁺ OPCs (Fig. 5D–H), suggesting that VLDLR may serve as the surface receptor for CLU-mediated OPC injury.

Excessive CLU induces OPC and myelin loss through inhibition of the PI3K-AKT pathway

Transcriptomic analysis indicated the inhibition of the PI3K-AKT signaling pathway upon CLU exposure (Supplementary Dataset 3). Subsequently, we investigated the role of the PI3K-AKT pathway in CLU-mediated OPC and myelin loss. Western blot analysis confirmed a time-dependent reduction in phosphorylated PI3K (p-PI3K), phosphorylated AKT (p-AKT), and phosphorylated mTOR (p-mTOR) levels following CLU stimulation in cultured OPCs (Fig. 6A–D). To explore this further, we utilized SC79, an AKT agonist, and MK2206, an AKT antagonist, to intervene in the CLU-mediated injury process. Results revealed that SC79 attenuated the loss of NG2⁺ OPCs and CCI⁺ OLs in the corpus callosum, indicating a protective effect against CLU-induced damage to the OPC lineage (CLU+SC79 vs. CLU+veh). Conversely, AKT inhibition by MK2206 further intensified CLU-induced damage to OPC lineage (CLU+MK2206 vs. CLU+veh, Fig. 6E–G). In addition, the proportions of CC3⁺ OPCs and CC3⁺ OLs were decreased by SC79 (CLU+SC79 vs. CLU+veh), whereas they were increased by MK2206 (CLU+MK2206 vs. CLU+veh, Fig. 6H, I). These findings highlight the role of CLU in promoting OPCs and OLs apoptosis through the inhibition of the PI3K-AKT-mTOR signaling pathway.

CLU knockdown enhanced remyelination in the corpus callosum

Given the direct deleterious effects of CLU, we explored the therapeutic potential of CLU inhibition. AAV carrying CLU-specific shRNA (AAV-shCLU-EGFP) or its scramble control (AAV-EGFP) was constructed (Fig. 7A) and injected into the corpus callosum via stereotaxic injection. After 3 weeks, an inflammatory demyelinating lesion was induced by LPC injection (Fig. 7B). Tissue samples were collected

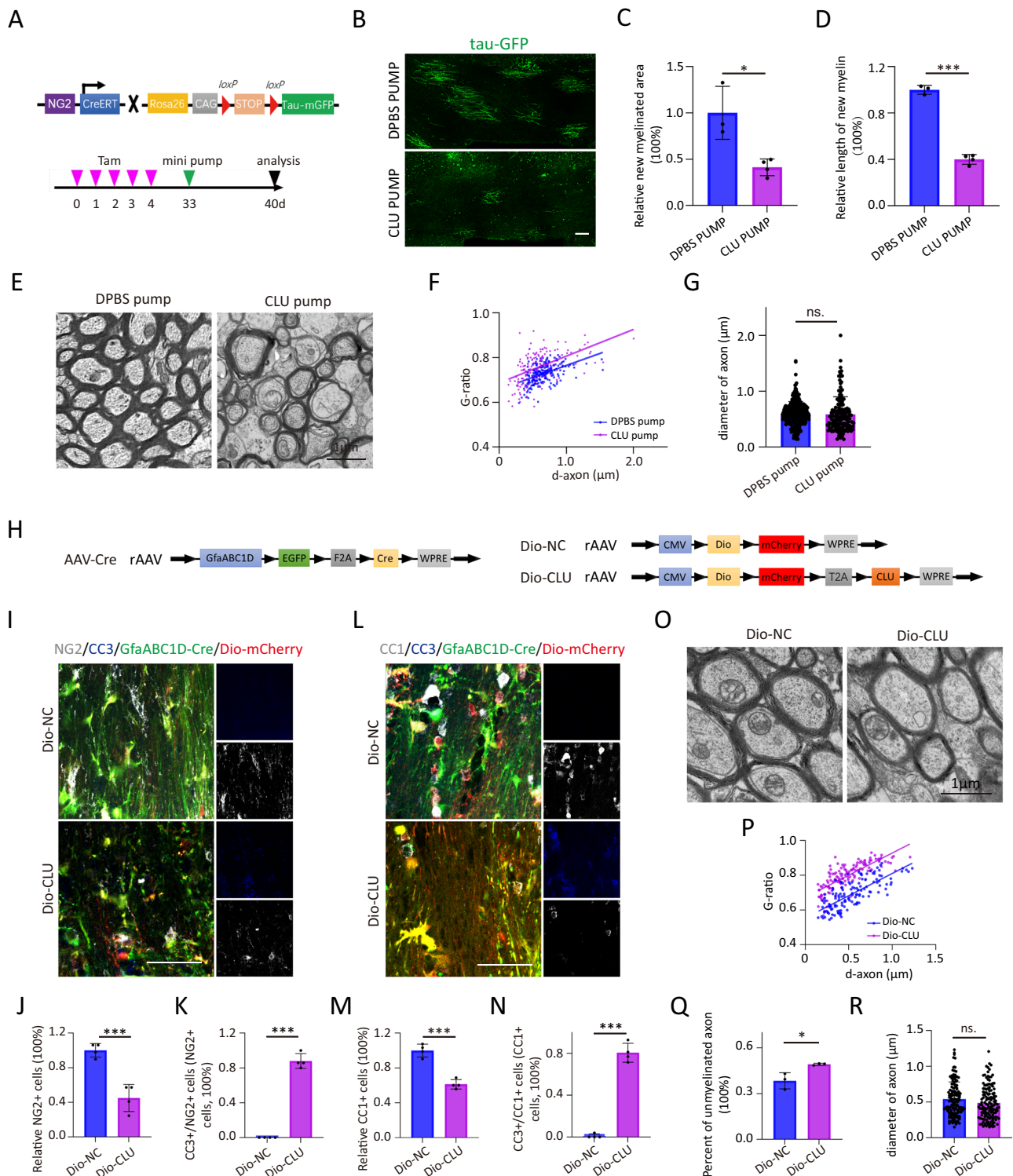


Fig. 4 | Impact of elevated CLU on OPC and myelin loss in the corpus callosum.

A Schematic representation of NG2-CreERT2::tau-mGFP reporter mice construction and experimental arrangement. **B–D** CLU administration into the corpus callosum for 7 days via implantable osmotic pumps significantly reduced the length of new myelin and the newly myelinated area, compared to DPBS vehicle control mice ($n = 4$ mice/group, $p = 0.0107$; $p > 0.0001$). Three independent experiments were conducted). **E, F** TEM revealed thinner myelin sheaths in CLU-administered mice compared to DPBS-administered mice. **G** No significant difference in axon diameter was observed between CLU-administered mice and DPBS-administered mice ($n = 3$ mice/group, $p = 0.5586$). **H** Schematic of viral constructs. **I–K** CLU upregulation by AAV significantly reduced the number of NG2⁺ OPCs and increased CC3⁺ OPCs

($n = 4$ mice/group, $p = 0.0007$; $p < 0.0001$). **L–N** CLU upregulation by AAV significantly reduced the number of CC1⁺ OLs and increased CC3⁺ OLs ($n = 4$ mice/group, $p = 0.0001$; $p < 0.0001$). **O, P** TEM uncovered a reduction in myelin sheath thickness in Dio-CLU mice relative to the Dio-NC group ($n = 3$, three independent experiments were conducted). **Q, R** The percentage of unmyelinated axons was elevated in Dio-CLU mice compared to the Dio-NC group ($n = 3$ mice/group, $p = 0.0241$), while the axon diameter was unchanged ($n = 3$ mice/group, $p = 0.0789$). For immunofluorescence pictures: Scale bar: 50 μm. For TEM: Scale bar: 1 μm. Statistical analysis was performed using unpaired two-tailed Student's *t*-tests, mean ± SD, * $p < 0.05$, ** $p < 0.01$, *** $p < 0.001$. ns. = *p* not significant. Tam tamoxifen.

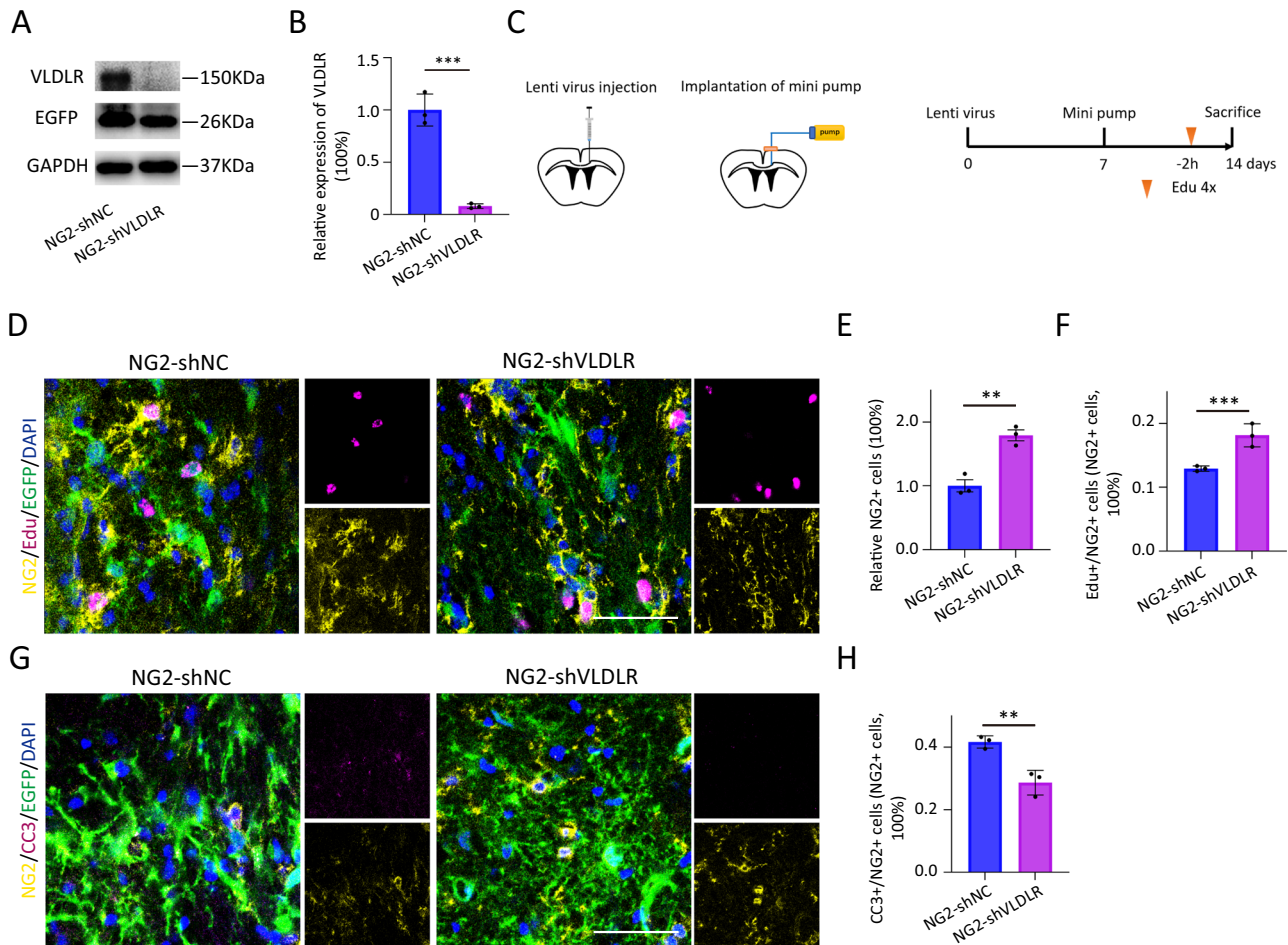


Fig. 5 | CLU-induced OPC injuries were attenuated by VLDLR knockdown in vivo. **A, B** NG2-shRNA-mediated VLDLR knockdown efficiency was determined by Western blot ($n = 3$ technical replicates/group, $p = 0.0005$). **C** Schematic of viral constructs and representation of the experimental setup. **D–F** The reductions of NG2⁺ OPCs and Edu⁺ OPCs in the CLU-administered group were reversed by VLDLR's specific knockdown of OPCs ($n = 3$ mice/group, $p = 0.0035$; $p = 0.0083$).

G, H The increase of CC3⁺ OPCs in the CLU-administered group was reversed by VLDLR's specific knockdown of OPCs ($n = 3$ mice/group, $p = 0.0070$). For immunofluorescence pictures: Scale bar: 50 μm . Statistical analysis was performed using unpaired two-tailed Student's *t*-tests, mean \pm SD, * $p < 0.05$, ** $p < 0.01$, *** $p < 0.001$. ns. = p not significant. VLDLR very low-density lipoprotein receptor.

at 5 days post-injection (dpi) (proliferation stage), 10 dpi (differentiation stage), and 21 dpi (remyelination stage) to analyze changes in OPC lineages and myelin sheaths.

Compared to the scramble control, AAV-shCLU-EGFP increased the number of NG2⁺ OPCs in the inflammatory demyelinating lesion. Proliferation ability was measured by injecting 4 \times BrdU before brain sample collection, revealing an elevated number of BrdU⁺/NG2⁺ OPCs in the lesion (Fig. 7C–E). This indicates that CLU knockdown promotes OPC proliferation in LPC models.

To track the OPC differentiation, OPCs were labeled with EdU before LPC injection. The numbers of NG2⁺ OPCs and CCI⁺ OLs in the lesion increased at dpi 10 (Fig. 7F–H). Additionally, EdU and CCI co-staining demonstrated an increase in Edu⁺/CCI⁺ OLs in the demyelinating lesion in AAV-shCLU mice, suggesting that more OPCs differentiated to OLs after CLU knockdown (Fig. 7I, J). TEM analysis further showed that the thickness of the myelin sheath increased after CLU knockdown compared to the scramble control, without influencing the axon diameter (Fig. 7K–M). The proportion of unmyelinated axons was increased in AAV-shCLU-EGFP injected mice compared with AAV-EGFP control mice (Fig. 7N). To assess the time course of LPC affected by AAV-shCLU-EGFP, a later time point was chosen (dpi 28). The results showed that the demyelinating area in AAV-shCLU-EGFP injected mice was smaller than in AAV-EGFP control mice, with higher MBP intensity (Supplementary Fig. 6A–C). These results demonstrate that CLU

knockdown restores the proliferation and differentiation abilities of OPCs, enhancing the process of remyelination in the corpus callosum.

Astrocyte-specific CLU conditional knockout improved myelin renewal

To validate the findings from CLU knockdown experiments, we generated ALDH1L1-CreERT::CLU^{fl/fl} mouse (Fig. 8A). LPC was injected after tamoxifen-induced Cre expression. Compared to CLU^{fl/fl} mice, CLU cKO^{AST} mice exhibited increased Olig2⁺ OPCs and CCI⁺ OLs in the corpus callosum (Fig. 8B–D). TEM studies further revealed thicker myelin sheaths and more myelinated axons in CLU cKO^{AST} mice compared to CLU^{fl/fl} mice (Fig. 8E–G). No difference in the axon diameter between the two groups was found (Fig. 8H).

To further investigate the effects of astrocyte-specific CLU deletion, we constructed AAV serotype 5-expressing Cre recombinase fused to EGFP (AAV-Cre-EGFP) or EGFP alone (AAV-EGFP) driven by the mouse GfaABC1D promoter (Supplementary Fig. 7A, B). The virus was injected into the corpus callosum of CLU^{fl/fl} mice, and LPC induced a demyelinating lesion. Tissues were collected at 10 dpi and 21 dpi. Similar to cKO mice, AAV-mediated CLU deletion in astrocytes increased the number of Olig2⁺ OPCs and CCI⁺ OLs (Supplementary Fig. 7C–E) and thickened myelin sheaths in the demyelinating lesion (Supplementary Fig. 7F, G). These results collectively demonstrate that the conditional knockout of the CLU gene in astrocytes promotes OPC

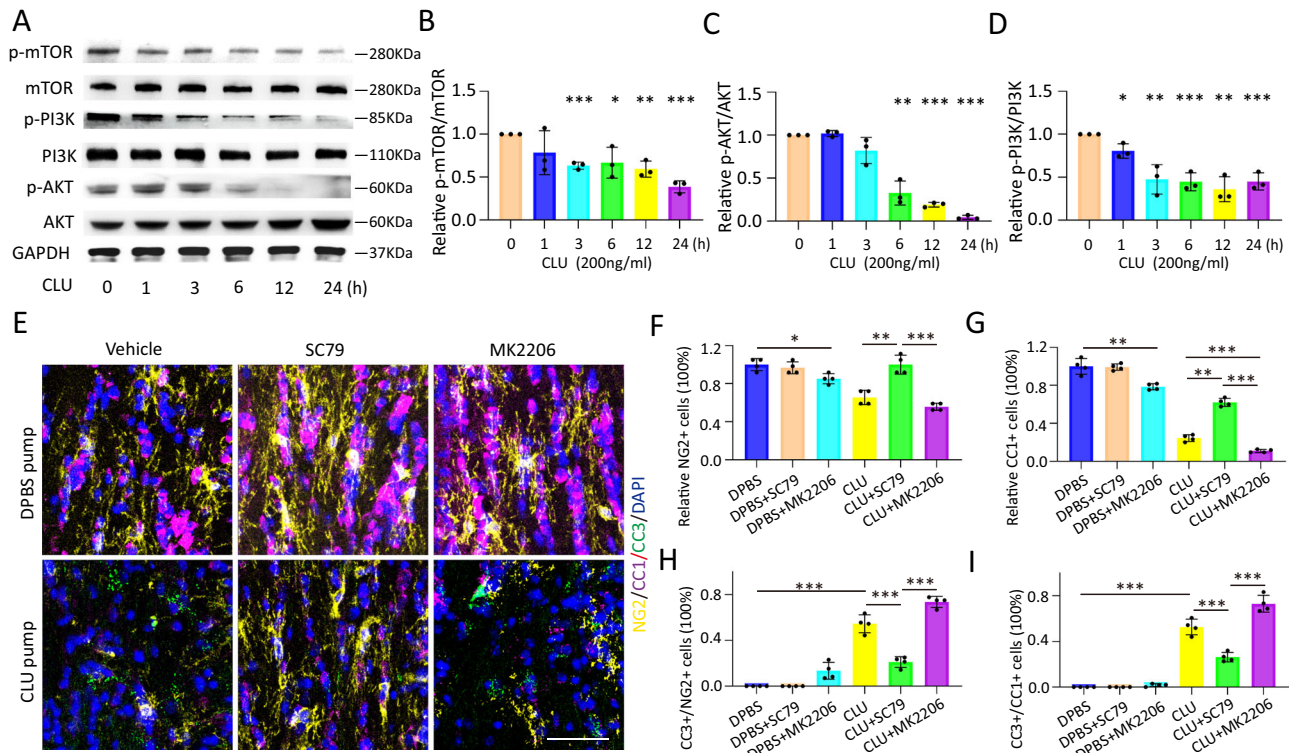


Fig. 6 | CLU-induced OPCs and OL injury through inhibition of the PI3K-AKT pathway. **A–D** Western blot confirmed a time-dependent reduction in p-PI3K, p-AKT, and p-mTOR after CLU stimulation ($n = 3$ technical replicates/group) (For p-mTOR/TOR, 1 h vs. 0 h $p = 0.2193$; 3 h vs. 0 h $p = 0.0001$; 6 h vs. 0 h $p = 0.0335$; 12 h vs. 0 h $p = 0.0017$; 24 h vs. 0 h $p = 0.0001$) (For p-AKT/AKT, 1 h vs. 0 h $p = 0.3765$; 3 h vs. 0 h $p = 0.1101$; 6 h vs. 0 h $p = 0.0011$; 12 h vs. 0 h $p < 0.0001$; 24 h vs. 0 h $p < 0.0001$) (For p-PI3K/PI3K, 1 h vs. 0 h $p = 0.0155$; 3 h vs. 0 h $p = 0.0061$; 6 h vs. 0 h $p < 0.0008$; 12 h vs. 0 h $p = 0.0016$; 24 h vs. 0 h $p = 0.0007$). **E–I** SC79 (an AKT agonist) could mitigate CLU damage to the OPC lineage, while MK2206 (an AKT antagonist) could exacerbate CLU damage to the OPC lineage in vivo ($n = 4$ mice/group) (For

(F), DPBS vs. DPBS+MK2206 $p = 0.0117$, CLU vs. CLU+SC79 $p = 0.0015$, CLU+SC79 vs. CLU+MK2206 $p = 0.0002$) (For (G), DPBS vs. DPBS+MK2206 $p = 0.0003$, CLU vs. CLU+SC79 $p < 0.0001$, CLU vs. CLU+MK2206 $p = 0.0005$, CLU+SC79 vs. CLU+MK2206 $p < 0.0001$) (For (H), DPBS vs. CLU $p < 0.0001$, CLU vs. CLU+SC79 $p = 0.0003$, CLU+SC79 vs. CLU+MK2206 $p < 0.0001$) (For (I), DPBS vs. CLU $p < 0.0001$, CLU vs. CLU+SC79 $p = 0.0006$, CLU+SC79 vs. CLU+MK2206 $p < 0.0001$). For immunofluorescence pictures: Scale bar: 50 μm . Statistical analysis was performed using unpaired two-tailed Student's t -tests, mean \pm SD. * $p < 0.05$, ** $p < 0.01$, *** $p < 0.001$. ns. = p not significant.

differentiation and remyelination in LPC-induced inflammatory demyelinating lesions.

The effects of conditional CLU knockout in astrocytes were also observed in the EAE mouse model. EAE was induced in CLU^{fl/fl} and CLU cKO^{AST} mice, as described above. Conditional knockout of CLU in astrocytes delayed EAE onset and reduced the clinical severity of EAE animals compared to CLU^{fl/fl} controls (Fig. 8I). At the peak of the disease onset, the spinal cord was collected to detect the OPC lineage cells. The results showed an increased number of OPCs in the spinal cord white matter of CLU cKO^{AST} mice (Fig. 8J, K, M). To evaluate the role of CLU in EAE mice, the proliferation (Ki67) and apoptosis (CC3) of OPCs were examined, revealing that CC3⁺ OPCs were reduced in CLU cKO^{AST} mice, compared to CLU^{fl/fl} controls, while no difference in Ki67⁺ OPCs was identified between the two groups (Fig. 8L, N). Additionally, the number of IBA1⁺ microglia/macrophages was reduced in the spinal cord white matter (Supplementary Fig. 7H, I). These findings indicate that the knockout of CLU in astrocytes plays a protective role in the EAE model.

Discussion

This study reveals that CLU protein is selectively increased in astrocytes within the active lesion area of patients with MS and animal models of demyelinating diseases. CLU exerts both autocrine and paracrine deleterious effects by inhibiting astrocytic phagocytosis of myelin debris and disrupting remyelination by OPCs, respectively. Administration of recombinant CLU protein significantly alters the

transcriptome of OPCs and inhibits OPC differentiation and survival through the inhibition of the PI3K-AKT signaling pathway in vitro and in vivo. Finally, the study demonstrates that knockdown and conditional knockout of astrocytic CLU can ameliorate pathological changes and clinical manifestations in animal models of demyelinating diseases, highlighting CLU as a therapeutic target for MS.

While it is acknowledged that different CLU isoforms exist with varying subcellular locations and molecular functions³⁴, CLU is generally considered a secreted molecular chaperone capable of binding to various extracellular molecules, ligands, and membrane receptors³⁴. Dysregulated CLU is implicated in the pathogenesis of several diseases, including cancers and neurodegenerative diseases. Variants in the CLU gene are recognized as strong dominant genetic factors in late-onset Alzheimer's disease (AD)^{35,36}. CLU's functional interactions with amyloid- β (A β) peptides contribute to AD pathology, impacting amyloidogenesis^{37,38} and A β deposition³⁹. The outcome of CLU-A β interaction is a complex one⁴⁰. Some studies suggest the potential benefits of astrocytic CLU overexpression in resolving AD pathology^{37,41}, while others propose that increased neuronal CLU expression enhances neuroinflammation and A β toxicity^{38,42,43}. Moreover, a recent study using iPSC-derived astrocytes indicated that compared to the T/T and C/T alleles, the C/C alleles at the rs11136000 loci, the third strongest genetic risk factor for AD, elevated CLU and inflammatory responses, inhibiting OPC proliferation and myelination⁴⁴. A diffusion tensor imaging study reported that healthy adults carrying C alleles in the CLU gene are linked to a lower fractional

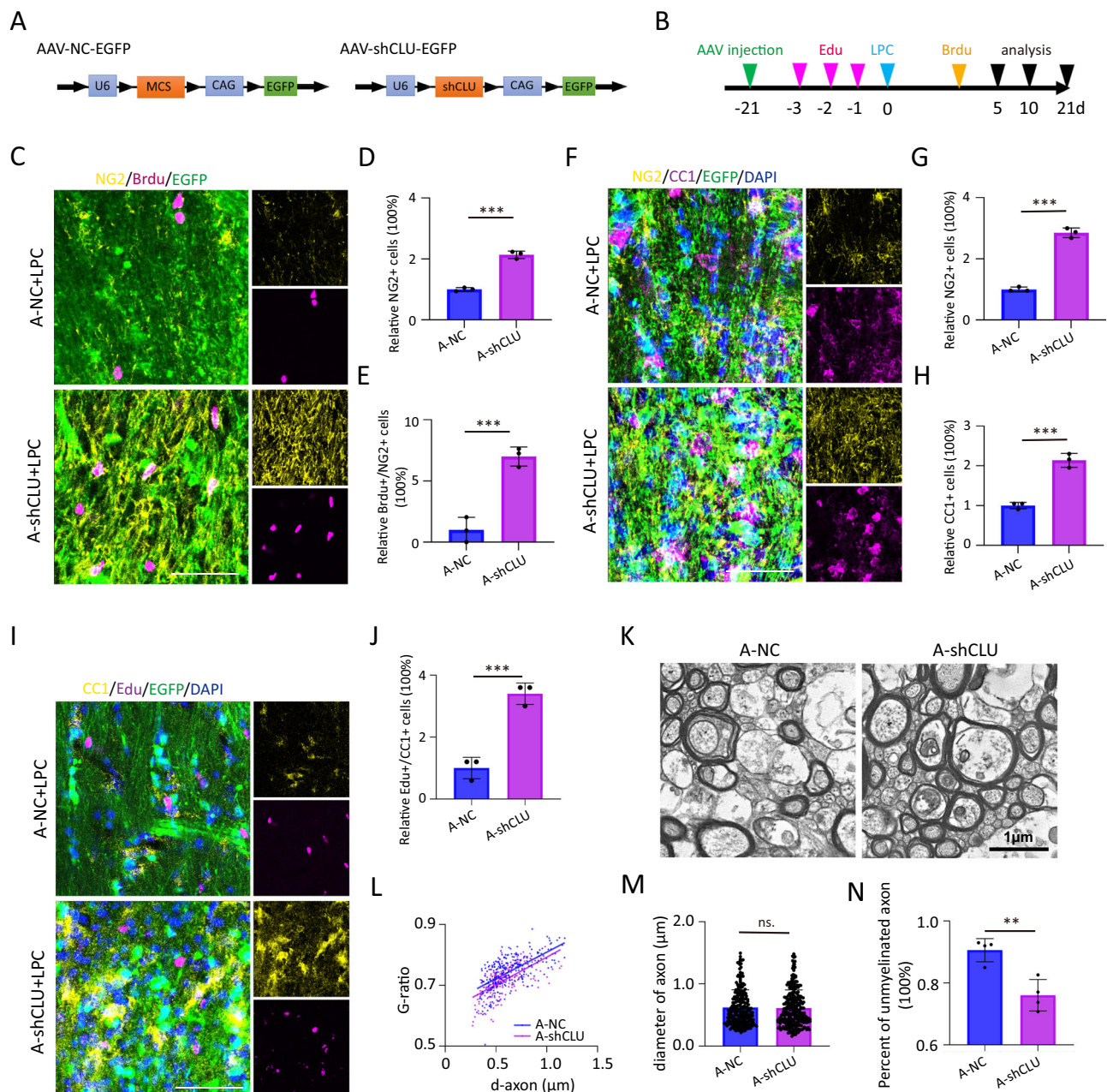


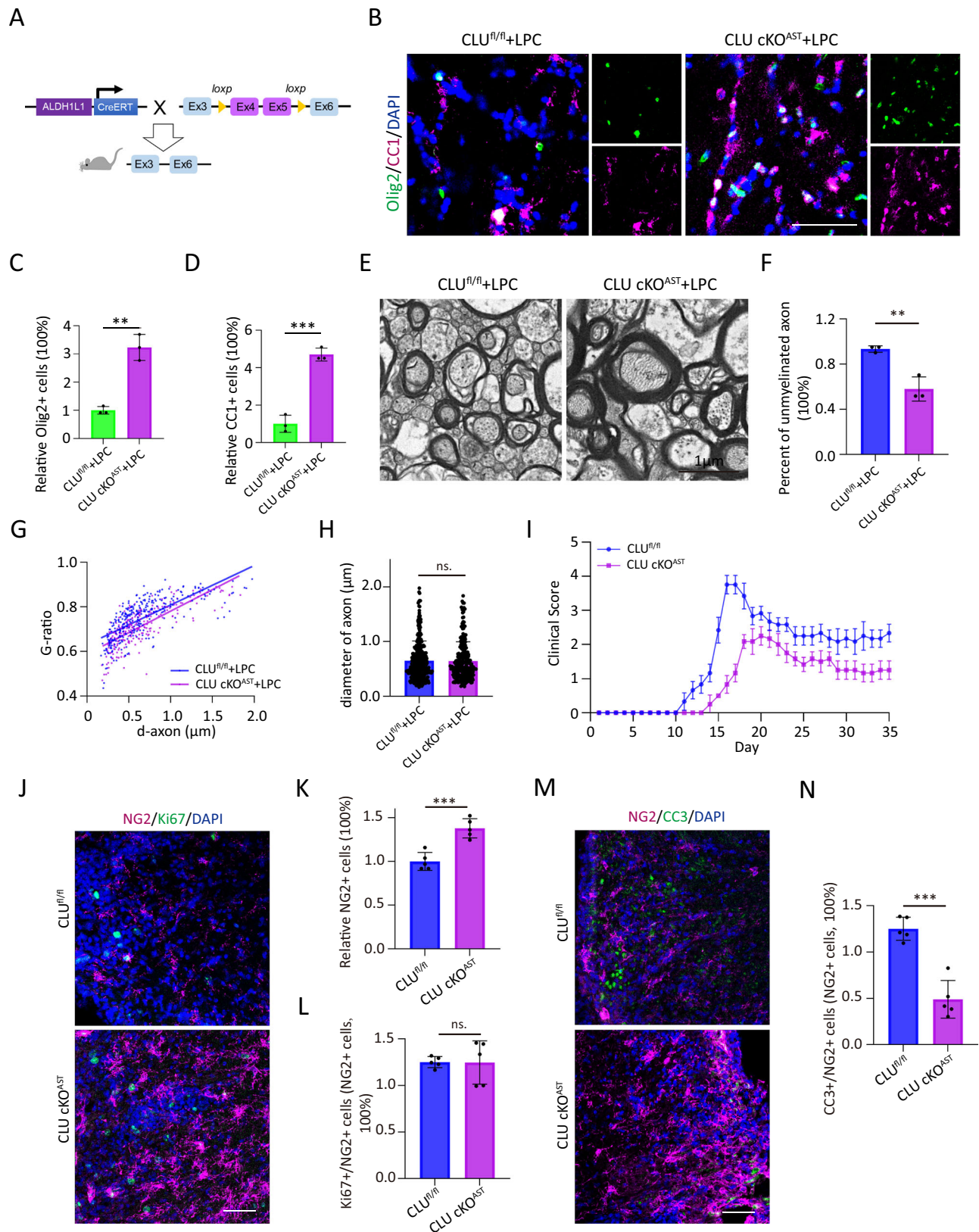
Fig. 7 | Enhanced remyelination in the corpus callosum with CLU knockdown in the LPC model. **A** Schematic of viral constructs. **B** Schematic representation of the experimental arrangement. **C–E** Increased proliferation ability of OPCs following CLU knockdown ($n = 3$ mice/group, $p = 0.0001$; $p = 0.0013$). **F–H** Increased numbers of NG2+ OPCs and CC1+ OLs after CLU knockdown ($n = 3$ mice/group, $p < 0.0001$; $p = 0.0005$). **I, J** Enhanced OPC differentiation ability after CLU knockdown, detected by Edu differentiation assay ($n = 3$ mice/group, $p = 0.0011$). **K, L** TEM analysis revealed increased myelin sheath thickness after CLU knockdown

($n = 4$ mice/group, three independent experiments were conducted). **M, N** The percentage of unmyelinated axons was decreased in A-shCLU mice compared to the A-shNC group ($n = 4$ mice/group, $p = 0.0037$), while the axon diameter was unchanged ($n = 4$ mice/group, $p = 0.6686$). For immunofluorescence pictures: Scale bar: 50 μm. For TEM Scale bar: 1 μm. Statistical analysis was performed using unpaired two-tailed Student's *t*-tests, mean ± SD, * $p < 0.05$, ** $p < 0.01$, *** $p < 0.001$. ns. = *p* not significant. LPC lyssolecithin, Edu 5-ethynyl-2'-deoxyuridine, BrdU 5-bromo-2'-deoxyuridine.

anisotropy, a marker tied to reduced white matter integrity and demyelination, in an allele dose-dependent manner⁴⁵. These studies support the deleterious role of CLU in AD. Notably, the study of functional SNPs in the *CLU* gene by Liu et al.⁴⁴ and Braskie et al.⁴⁴ neglects Aβ pathology with emphasis on myelination. MS and demyelinating disease animal models are irrelevant to Aβ, while dysfunctional OPCs represent a hallmark of the disease. Our data were consistent with AD studies demonstrating that continuous delivery of excessive recombinant CLU protein reduced OPC survival, differentiation, and myelination in vivo, while depletion or silencing of CLU

in astrocytes restored OLs differentiation and myelin sheath formation in two animal models of MS. The current study provided evidence for the detrimental role of CLU through its impeding of OPC-mediated remyelination in demyelinating diseases, underscoring CLU as a therapeutic target for MS.

Astrocytes are phagocytes that can compensate for microglia/macrophages to clear cell debris⁴⁶. In demyelinating pathologies, astrocytes could serve as phagocytes to directly remove myelin debris via the endosomal-lysosomal system^{13,47}, in which the low-density lipoprotein receptor-related protein 1 (LRP1)⁴⁸ and the intracellular



interacting protein lipocalin-2 (LCN2)²⁷ are required for myelin debris binding and endocytosis. Conversely, CLU has been previously demonstrated to facilitate the ligand interaction of LRP1⁴⁹ (e.g., extracellular heat shock protein 90 alpha) and LRP2⁵⁰ (e.g., A β peptide) acting as a component of the ligand-receptor complex. Therefore, as a binding substrate of myelin-related lipids^{51–53} and

LRP^{54,55}, it is likely that CLU may promote myelin-LRP1 interaction. However, this contradicts our current findings, which suggest that CLU inhibits astrocytic phagocytosis of myelin debris. One explanation for the controversy is that CLU can act in various modes in distinct ratios relative to its receptor⁵⁶. Alternatively, instead of debris uptake, GSEA of astrocyte transcriptome indicated that CLU might also inhibit the

Fig. 8 | Improved myelin renewal with astrocyte-specific CLU conditional knockout in LPC and EAE models. **A** Schematic representation of the ALDH1L1-CreERT::CLU^{fl/fl} mice construction. **B–D** Increased numbers of Olig2⁺ OPCs and CC1⁺ OLs in the corpus callosum of CLU cKO^{AST} mice in the LPC model ($n = 3$ mice/group, $p = 0.0013$; $p = 0.0004$). **E–H** TEM analyses revealed thicker myelin sheaths in CLU cKO^{AST} mice compared to CLU^{fl/fl} mice. The percentage of unmyelinated axons decreased in CLU cKO^{AST} mice compared to the CLU^{fl/fl} group ($n = 3$ mice/group, $p = 0.0052$), while the axon diameter remained consistent ($n = 3$ mice/group, $p = 0.8429$). **I** Astrocyte-specific CLU conditional knockout decreased the

clinical severity of EAE animals ($n = 6$ mice/group). **J–L** Astrocyte-specific CLU conditional knockout increased the number of NG2⁺ OPCs at the peak of the disease onset, while the number of Ki67⁺ OPCs was unchanged ($n = 5$ mice/group, $p = 0.0005$; $p = 0.9679$). **M, N** Astrocyte-specific CLU conditional knockout increased the number of CC3⁺ OPCs at the peak of the disease onset ($n = 5$ mice/group, $p < 0.0001$). For immunofluorescence pictures: Scale bar: 50 μm . For TEM Scale bar: 1 μm . Statistical analysis was performed using unpaired two-tailed Student's *t*-tests, mean \pm SD, * $p < 0.05$, ** $p < 0.01$, *** $p < 0.001$. ns. = p not significant. LPC lysoclethrin.

intracellular lipid degradation pathway (*Lipid catabolic process*, normalized enriched score: -2.08 , CLU vs. vehicle, Supplementary Dataset 5), which is involved in astrocyte-mediated clearance of myelin debris¹³. Further investigation focusing on diverse aspects of astrocytic phagocytosis following CLU exposure is needed and may provide insights into the molecular mechanisms of CLU action.

Recently, the focus of MS research has been the contributions of multiple glial cell types to the development, progression, or amelioration of disease states. OPCs are specialized glial cells responsible for synthesizing myelin sheaths, enabling saltatory conduction, and providing metabolic support to neurons⁵⁷. In MS, inflammation routinely damages OPCs and OLs, causing demyelination and, consequently, axonal loss⁵⁸. OPCs must be recruited to the zone of myelin loss and undergo differentiation and maturation to become fully competent myelin-producing oligodendrocytes^{59,60}. However, the differentiation process of OPCs into mature myelin-producing oligodendrocytes is impaired in MS lesions due to the inflammatory microenvironment and many inhibitory molecules, which may cause inefficient remyelination⁶¹. The current study observed elevated astrocytic CLU in the lesions of EAE and LPC inflammatory demyelinating models. In contrast, in cuprizone-induced demyelination models, early-stage CLU was not altered in astrocytes or other neuronal cells. Notably, transcriptomic analysis of CLU-treated astrocytes and OPCs (3 h and 24 h) did not possess altered inflammatory mediators (e.g., cytokines and chemokines) and neuroinflammation-related signaling pathways. We propose that CLU can be strongly induced by neuroinflammation, while CLU per se has a moderate effect on neuroinflammation in our experimental settings. Instead, CLU can inhibit OPC proliferation, differentiation, survival, and myelin sheath formation in cell cultures and organoids. CLU acts as a neuroinflammation surrogate molecule that is inducible by inflammatory responses and executes inflammation-induced demyelination and impaired remyelination by directly acting on OPCs.

CLU elevation was observed in the LPC and EAE models, but surprisingly not in the cuprizone models. This may be attributed to a potential model-dependent mechanism. For example, the timing of glia reactivation and immune cell infiltration differs between models, occurring within days in the LPC model, while taking weeks in the cuprizone model. In the cuprizone model, demyelination typically occurs earlier than significant astrocyte reactivation, which peaks after approximately 5 weeks⁶². The infiltration of T cells also lags behind and becomes significant after about 4 weeks⁶². Additionally, the targets of toxic agents vary. LPC disrupts the myelin sheath, whereas cuprizone impairs mitochondrial function, potentially leading to different compositions of demyelinating debris. Furthermore, by chelating copper, cuprizone may also directly affect other cell types, including astrocytes⁶³. These differences between the two models could result in distinct patterns of gene dysregulation and transformations within astrocyte clusters or states. Future studies that compare the differential responses in astrocytes between the two models may provide insight into the mechanisms underlying CLU elevation.

This study has limitations. In the studies with excessive CLU, delivered by either recombinant protein or virus-mediated overexpression, deleterious effects on myelin thickness were demonstrated. Given that CLU exhibits harmful effects on OLs and OPCs,

these data suggested that changes in myelin thickness could result from a complex relationship between demyelination and delayed new myelin formation following CLU exposure. Since CLU is continuously released and active in our setting, causing ongoing death of OPCs and OLs, it is difficult to quantify the relative contributions of demyelination and remyelination by CLU in vivo. Nevertheless, the study demonstrated a multifaceted pathogenic role of CLU and proposed CLU as a druggable target for demyelinating diseases to retard demyelination and promote recovery.

In conclusion, the current study supports the notion that CLU is an inducible astrocyte-derived factor for MS pathology by exerting autocrine and paracrine deleterious effects to disrupt astrocytic removal of myelin debris, promote OLs death, and interfere with OPCs function during demyelination and remyelination.

Methods

Human brain specimens

Brain biopsies were obtained from two cases employing a standard neurosurgical procedure. The specimens were dissected and flash-frozen in liquid nitrogen and stored at -80 °C prior to further processing for immunofluorescence staining (outlined below). The sampling locations have been highlighted in Fig. 1A. The written informed consent was obtained by each donor for the use of the human samples and information of participants, including age, gender, diagnosis and medical center the participants attended. Detailed information associated with the participants was summarized in Supplementary Table 1. The study was approved by the Ethics Committee of The Third Affiliated Hospital of Sun Yat-sen University (Approval Number: [2021]02-250-01).

Animals

Experimental procedures complied with all the relevant ethical regulations and were approved by the Ethics Committee of South China Agricultural University (Approval Number: 2020B041). NG2-CreERT mice (The Jackson Laboratory, Cat: 008538) were bred with Tau^{mGFP} mice (The Jackson Laboratory, Cat: 021162. mGFP refers to membrane-bound green fluorescent protein) to generate NG2-CreERT::Tau^{mGFP} mice. To create astrocyte-specific CLU conditional knockout mice, Aldh1l1-CreERT mice (The Jackson Laboratory, Cat: 029655) were crossed with the CLU^{fl/fl} mice to produce Aldh1l1-CreERT::CLU^{fl/fl} mice. The NG2-CreERT and Tau^{mGFP} mice were gifts from Professor Feng Mei of the Third Military Medical University⁶⁴. The Aldh1l1-CreERT mice were gifts from Professor Ke Li of the Guangdong Laboratory Animals Monitoring Institute. Mice were maintained in a C57BL/6 background and inter-crossed to produce offspring for subsequent experiments. CLU^{fl/fl} mice were acquired from Shanghai Model Organisms Center, Inc. and bred at the Experimental Animal Center of South China Agricultural University. Seven-week-old female wild-type C57BL/6j mice (18–20 g) were purchased from Guangdong Gem-Pharmatech Co., Ltd. Animals were housed in isolation cages at a temperature of 22 ± 2 °C and humidity of $55 \pm 5\%$ under specific pathogen-free conditions, under a 12-h light/12-h dark cycle and access to water and food ad libitum. Mice were anesthetized with 1% pentobarbital for further experiments.

Antibodies and viruses

All antibodies and viruses utilized in this study are listed in Supplementary Table 2.

Primary astrocyte culture

Primary astrocyte cultures were generated from cerebral cortices of P0 C57BL/6 pups using slight modifications^{65–67}. Specifically, after carefully removing the meninges from the cortices, the remaining tissues were dispersed and digested using 0.25% trypsin-EDTA (Sigma-Aldrich, cat: T4049) in a rocking water bath at 37 °C for 20 min. The digestion process was halted by adding DMEM/F12 (Invitrogen, cat: 11320033) medium supplemented with 10% FBS. The enzymatically dissociated cells were filtered through a 70 µm cell strainer and rinsed with DMEM/F12 medium. The primary cortical culture of a single mouse was cultured in isolation in a T25 flask with 6 mL of astrocyte-specific medium supplemented with DMEM/F12 (Sigma-Aldrich, cat: D843), 1% non-essential Amino Acids (Gibco, cat: 11140050), 1.6 mM L-glutamine (ThermoFisher, cat: 25030081), 10% fetal bovine serum (PAN, cat: ST30-3302), 0.2 mM Pyruvic acid sodium (Sigma-Aldrich, cat: S8636), and 1% penicillin-streptomycin (Millipore, cat: 516106). Media was supplemented on the 2nd day and replaced every 3 days. Following 1 week of growth, the flasks were transported to a heated (37 °C) shaker for 18 h to purify astrocytes. Microglia and OPCs developing above the layer of astrocytes were shaken off. Purified astrocytes within three passages were utilized for experiments.

Generation of neural progenitor cell-derived OPCs

Progenitor-derived OPCs were obtained using neural progenitor cells (NPCs) from the cerebral cortices of postnatal day 0 C57BL/6 mouse pups. The cerebral cortices were digested with trypsin (Gibco, cat: 25200072) at room temperature for 20 min. The single cell suspension was cultured in NPC culture medium, supplemented with neurobasal medium (Gibco, cat: 21103049), 2% B27 (Gibco, cat: 17504044), 20 ng/mL epidermal growth factor (PeproTech, cat: AF-100-15), 20 ng/mL basal fibroblast growth factor (PeproTech, cat: 100-18B), 1.6 mM L-glutamine (ThermoFisher, cat: 25030081), and 1% penicillin-streptomycin (Millipore, cat: 516106). The generated neurospheres were passaged every 3 days, and the third passage was employed for OPC induction. For OPC differentiation, NPCs (1×10^4 per well) were allowed to adhere to 24-well plates coated with 0.1 mg/mL Poly-D-Lysine (Sigma-Aldrich, cat: P0899) with OPC culture medium, supplemented with neurobasal medium, 2% B27, 10 ng/mL basal fibroblast growth factor, 10 ng/mL, platelet-derived growth factor-AA (PeproTech, cat: 315-17), and 1% penicillin-streptomycin. Following 2 days of induction, OPCs were incubated in a differentiation medium containing neurobasal medium, 2% B27, and 1% penicillin-streptomycin. Cell slides were processed for immunostaining 5 days after differentiation, and MBP-positive cells were counted. For proliferation and apoptosis experiments, NPC-derived OPCs were grown in an OPC medium throughout the experiments.

Microglia isolation and purification

Primary microglia cultures were established from postnatal P0 C57BL/6j mouse pups. The forebrains of the pups were isolated and dissociated in 0.25% trypsin containing 100 µL/mL DNase I (Invitrogen, cat: 18047019) for 15 min at 37 °C. The cell suspension was passed through a 70 µm cell strainer, and the cells were collected by centrifugation at $170 \times g$ for 10 min at room temperature. The cells were then washed with DMEM and seeded at a density of 2 forebrains per T75 flask in a complete DMEM culture medium supplemented with 10% FBS and 1% penicillin-streptomycin. Half of the medium was replaced every 2 days. When the astrocytes reached confluence, microglia were isolated using the shake-off method by incubating the flasks at 200 rpm for 2 h at 37 °C. The detached microglia were collected by centrifugation at $170 \times g$ for 10 min at room temperature, suspended in

complete DMEM culture medium supplemented with 30% L929 conditioned medium, and then seeded at a density of 250,000 cells per well in poly-D-lysine-coated containers for subsequent experiments.

Organotypic brain slice culture

Brain tissue was harvested from postnatal day seven C57BL/6 mice, and transverse sections (350 µm thickness) of the cerebellum were acquired using a microslicer (Cavey Laboratory Engineering). Usually, 4–5 randomly collected slices were placed in an upper chamber of a transparent coated membrane insert (Corning, cat: 3450) containing 1 mL of culture medium per well in the lower chamber, containing 50% minimum essential medium (Gibco, cat: C11095500BT), 25% HBSS (Gibco, cat: 14170120), 25% horse serum (Invitrogen, cat: 16050122), 28 mM D-glucose (Sigma-Aldrich, cat: G8644), 2 mM glutamine (Gibco, cat: 25030081), and 1% penicillin-streptomycin. The brain slices were maintained in a humidified atmosphere with 5% CO₂ at 37 °C, and the culture medium was cycled every 2 days. Experiments commenced after another 3 days of recovery from growth.

Myelin phagocytosis assay

Myelin was isolated from adult mouse brain tissue using density gradient centrifugation in 30% Percoll (Cytiva, cat: 17089101). The concentration of myelin protein was quantified using the BCA protein assay kit (KeyGEN BioTECH, cat: KGB2101). To assess the phagocytic capacity and extent of myelin phagocytosis, myelin was labeled with fluorescent dyes 1,19-dioctadecyl-3,3,39,39-tetramethylindocarbocyanine perchlorate (DiI; Invitrogen, cat: D282) or CFSE (Invitrogen, cat: 65-0850-84) at 37 °C for 30 min. Astrocytes and microglia were exposed to 200 µg/mL DiI/CFSE-labeled myelin for 1.5 h, fluorescence intensity was measured using the FACS Calibur (BD Biosciences). Additionally, astrocytes and microglia were stained with LysoTracker™ Red DND-99 (Invitrogen, cat: L7528) at 37 °C for 30 min to analyze myelin-lysosome colocalization using TCS SP8 microscopy (Leica).

Electron microscopy

Mice were deeply anesthetized using 1% pentobarbital and perfused with pre-cold PBS to rinse the blood, followed by 2.5% glutaraldehyde for primary tissue fixation. The brain was dissected immediately and post-fixed with 2.5% glutaraldehyde overnight at 4 °C. Samples were washed and treated with 1% osmium tetroxide, dehydrated, and embedded in Epon 812. The ultrathin tissue sections were obtained using an ultramicrotome (Leica, EM UC-7) and stained using 2% uranyl acetate and 3% lead citrate. After washing with purified water, the sections were imaged utilizing a transmission electron microscope (HITACHI, HT7800, 120kv). Each myelin sheath was traced using the ImageJ freehand drawing tool, and the G-ratio was determined for comparisons between groups.

The experimental autoimmune encephalomyelitis (EAE) model

The 8- to 10-week-old female Aldh1l1-CreERT::CLU^{fl/fl} mice, CLU^{fl/fl} mice, and wild-type C57BL/6J mice were used to induce EAE. Each mouse was immunized via subcutaneous injection at the base of the tail with 200 µL of emulsions comprised of equal amounts of complete Freund's adjuvant (CFA) with 5 mg/mL *Mycobacterium tuberculosis* H37Ra (BD, cat: 231141) and 200 µg myelin oligodendrocyte glycoprotein (Scilight-Peptide, cat: c213426) in PBS. Pertussis toxin (200 ng per mouse, Sigma-Aldrich, cat: P7208) was administered intraperitoneally on days 0 and 2 following immunization. Mice were examined daily for clinical signs of EAE in a blinded fashion. The EAE score was assessed using a grading scale as follows: 0—normal; 0.5—partial tail paralysis; 1—tail paralysis; 1.5—reversible corrective reflex impairment; 2—corrective reflex impairment; 2.5—one hindlimb paralysis; 3—both hindlimbs paralysis; 3.5—both hindlimbs paralysis and one forelimb paralysis; 4—completely paralyzed limb; and 5—death.

Cuprizone model of demyelination

Demyelination was induced in 8-week-old female mice by feeding them a diet containing 0.2% cuprizone (Sigma-Aldrich, cat: C9012) for 5 weeks. Age- and sex-matched control mice were maintained on a normal diet, with food pellets changed every other day. After 5 weeks, the mice were sacrificed to assess the extent and effects of demyelination.

Drug treatment

For AKT interference, mice were injected with 2 mg/kg of SC79 (a specific AKT agonist, MCE, cat: HY-18749) intraperitoneally or provided with 40 mg/kg MK-2206 dihydrochloride (a selective allosteric AKT inhibitor, MCE, cat: HY-10358) orally from the day of the miniosmotic pump installation. The drugs were administered once daily for seven consecutive days. To modulate SIPRI signaling, mice were given 10 mg/kg SEW2871 (an SIPRI agonist, MCE, cat: HY-W008947) orally or 1 mg/kg Siponimod (an active and selective SIP receptor modulator, MCE, HY-12355) once a day for seven consecutive days from the day of the miniosmotic pump installation.

Administration of tamoxifen

Tamoxifen (MCE, cat: HY-13757A) was dissolved in corn oil at a concentration of 20 mg/mL. Eight-week-old NG2-CreERT::Tau-mGFP mice and Aldh1l1-CreERT::CLU^{fl/fl} mice were administered the tamoxifen solution at a dose of 100 mg/kg per day by oral gavage for 5 days to cause recombination. The Cre and CLU^{fl/fl} littermates received identical tamoxifen treatment as controls. Five days after the last tamoxifen administration, the mice were utilized for subsequent experiments.

BrdU and Edu administration and labeling

BrdU (MCE, cat: HY-15910) and Edu (MACKLIN, cat: E832486) were utilized to assess OPC proliferation and differentiation, respectively. To characterize OPC proliferation *in vivo*, 200 µg/g (gram, body weight, i.p.) of BrdU was given 2 h before sacrifice. For differentiation assessment *in vivo*, mice were provided with 100 µg/g (gram, body weight, i.p.) of Edu for five consecutive days prior to the operation. For *in vitro* assays, Edu (20 µM, final concentration) was added into the OPC culture medium 4 h before cell harvest. Edu labeling was conducted strictly following the manufacturer's directions (Beyotime, cat: C00755). BrdU labeling was performed after tissue sections were collected. Specifically, sections were incubated in 2 M HCl for 30 min at 37 °C and stabilized in borate buffer (0.1 M, pH 8.0) for 20 min at room temperature. After BrdU was exposed, the sections were permeabilized and blocked in a blocking buffer (containing 0.25% Triton X-100 and 3% goat serum in PBS) for 1 h at room temperature. The sections were incubated at 4 °C overnight with primary antibodies (chicken anti-BrdU, 1:1000). After the sections were washed with PBS, the sections were incubated with secondary antibody conjugated to AlexaFluor 488 (goat anti-Chicken IgY, 1:1000, Invitrogen). Images were captured using an inverted fluorescence microscope (ZEISS, Axio Observer 3), and cells were counted using ImageJ software.

Western blotting

OPCs were scraped with cell lysis buffer containing a 1% Protease Inhibitor Cocktail (MCE, cat: HY-K0010) and a 1% Phosphatase Inhibitor Cocktail (MCE, cat: HY-K0022). The lysates were incubated on ice for 30 min and centrifuged at 10,000×g for 10 min to eliminate cellular debris. The protein concentration was examined using a BCA protein quantitation kit (KeyGEN BioTECH, cat: KGPBCA). The lysates were adjusted to the same protein concentration and combined with SDS-PAGE Sample Loading Buffer (Beyotime, cat: P0015). Protein electrophoresis was carried out using FuturePAGE™ precast gels (ACE, cat: ET15420LGel) at 130 V supplied by a Bio-Rad power source. The proteins were transferred to PVDF membranes (Millipore, cat: ISEQ00010) at 100 V and 300 mA. A Multicolor Prestained Protein Ladder

10–250 kDa (Epizyme Biotech, cat: WJ102) was used as a standard for protein size assessment. The transferred membranes were blocked in 5% milk in TBST for 1 h at room temperature and maintained with primary antibodies overnight at 4 °C. The membranes were washed with TBST and incubated with secondary antibody-conjugated horseradish peroxidase for 1 h at room temperature. The images were exposed using a chemiluminescent detection substrate (Millipore, cat: WBKLS) on a Bio-Rad ChemiDoc MP Imaging System.

Immunofluorescence staining

Mice were deeply anesthetized using an intraperitoneal overdose injection of sodium pentobarbital and transcardially perfused with cold phosphate-buffered saline (PBS, Sangon Biotech, cat: A610100) followed by 4% (w/v) paraformaldehyde solution (PFA, Sangon Biotech, cat: E672002). Next, the brain and spinal cord were dissected, post-fixed in 4% PFA for 24 h, and immersed in sucrose (Sangon Biotech, cat: A100335) gradients (10%, 20%, and 30%) made in PBS at 4 °C for 48 h. The dehydrated tissues were frozen in OCT (Sakura, cat: 4583) and sectioned into coronal sections (30 µm) on a microtome cryostat (Leica, CM 1950). The sections were rinsed with PBS, permeabilized, and blocked using blocking buffer (containing 0.25% Triton X-100 and 3% donkey/goat serum in PBS) for 1 h at room temperature. The sections were incubated with primary antibodies overnight at 4 °C. After washing three times with PBS, the sections were incubated with the secondary antibody for 1 h at room temperature, and the nuclei were counterstained using DAPI for 10 min and mounted using a mounting medium. For immunocytochemistry, cell slides were fixed with 4% PFA for 30 min at room temperature, followed by a similar procedure as for tissue sections. Immunofluorescence images were acquired using a confocal microscope (Leica TSC SP8), and the fluorescence intensity was determined using ImageJ software.

LPC and virus injection

Mice were deeply anesthetized using 1% pentobarbital (i.p.) and immobilized on a stereotaxic frame (RWD Life Science). Mouse scalps were disinfected and incised along the midline to expose the skull. A burr hole (1 mm in diameter) was drilled by using a high-speed drill (RWD Life Science). LPC (1 µL, 1%, dissolved in 0.9% NaCl, Sigma-Aldrich, cat: L4129), lentivirus (1 µL), or AAV (1 µL) were stereotaxically injected at a rate of 0.2 µL/min bilaterally into the corpus callosum of 8- to 10-week-old mice using a Hamilton syringe. Injections were performed using a stereotaxic apparatus at the following coordinates: 0.6 mm anterior and 1.0 mm lateral to bregma at a depth of 1.8 mm. The date of injection was noted as 0 days post-injection (dpi). Following the injection, mice were maintained for immunohistochemical analysis for 5, 10, or 21 days before perfusion.

Miniosmotic pump installation

Mice were deeply anesthetized using 1% pentobarbital. Miniosmotic pumps (RWD, cat: 1001W, for continuous dosing over 7 days) were assembled using a brain infusion kit (RWD, cat: bic-3). The catheter tubing and miniosmotic pumps were preloaded with 10 ng/mL CLU (dissolved in DPBS) or DPBS and maintained overnight at 37 °C in 0.9% saline to initiate pumping. The miniosmotic pumps were installed in the subcutaneous pocket at the base of the notum, and the catheter tubing and cannula were guided to the initial injection site. The cannula was inserted at the following coordinates: 0.6 mm anterior and 1.0 mm lateral to bregma. The cyanoacrylate tissue adhesive (Durect, cat: 0008670) was employed to attach the cannula to the skull. The brains were collected for immunohistochemical analysis after the injection.

Statistical analysis

All statistical analyses were conducted using GraphPad Prism (version 9.0; GraphPad Software, Inc.). There were no computational methods

to determine the sample size a priori. Instead, sample sizes were selected based on similar studies. The data are presented as Mean \pm Standard Deviation (SD) across more than 3 experimental replicates/groups. All independent replicates were biological replicates, except data in Fig. 1B. Unless otherwise indicated, unpaired two-tailed Student's *t*-tests were performed to compare two groups with 95% confidence. A *p* < 0.05 was considered to be statistically significant. * indicates a *p*-value < 0.05, ** indicates a *p*-value < 0.01, *** indicates a *p*-value < 0.001. ns. indicates that the *p*-value was not significant.

Reporting summary

Further information on research design is available in the Nature Portfolio Reporting Summary linked to this article.

Data availability

The RNA-seq data generated in this study have been deposited in the NCBI Gene Expression Omnibus (GEO) database under accession code [GSE275514](https://www.ncbi.nlm.nih.gov/geo/query/acc.cgi?acc=GSE275514). Any additional requests for information can be directed to, and will be fulfilled by, the corresponding authors. Source data are provided with this paper.

Code availability

Codes used in this manuscript can be downloaded at <https://doi.org/10.5281/zenodo.12785154>.

References

- Franklin, R. & Ffrench-Constant, C. Regenerating CNS myelin—from mechanisms to experimental medicines. *Nat. Rev. Neurosci.* **18**, 753–769 (2017).
- Kihara, Y. & Chun, J. Molecular and neuroimmune pharmacology of S1P receptor modulators and other disease-modifying therapies for multiple sclerosis. *Pharmacol. Ther.* **246**, 108432 (2023).
- Colombo, E. & Farina, C. Lessons from S1P receptor targeting in multiple sclerosis. *Pharmacol. Ther.* **230**, 107971 (2022).
- Lunemann, J. D. et al. Correction: Immune reconstitution therapies: concepts for durable remission in multiple sclerosis. *Nat. Rev. Neurol.* **16**, 125 (2020).
- Włodarczyk, A. et al. A novel microglial subset plays a key role in myelinogenesis in developing brain. *EMBO J.* **36**, 3292–3308 (2017).
- Hagemeyer, N. et al. Microglia contribute to normal myelinogenesis and to oligodendrocyte progenitor maintenance during adulthood. *Acta Neuropathol.* **134**, 441–458 (2017).
- Absinta, M. et al. A lymphocyte-microglia-astrocyte axis in chronic active multiple sclerosis. *Nature* **597**, 709–714 (2021).
- Molina-Gonzalez, I. et al. Astrocyte-oligodendrocyte interaction regulates central nervous system regeneration. *Nat. Commun.* **14**, 3372 (2023).
- Endo, F. et al. Molecular basis of astrocyte diversity and morphology across the CNS in health and disease. *Science* **378**, c9020 (2022).
- Brandebura, A. N., Paumier, A., Onur, T. S. & Allen, N. J. Astrocyte contribution to dysfunction, risk and progression in neurodegenerative disorders. *Nat. Rev. Neurosci.* **24**, 23–39 (2023).
- Hammond, T. R. et al. Astrocyte-derived endothelin-1 inhibits remyelination through notch activation. *Neuron* **81**, 588–602 (2014).
- Morcos, Y., Lee, S. M. & Levin, M. C. A role for hypertrophic astrocytes and astrocyte precursors in a case of rapidly progressive multiple sclerosis. *Mult. Scler. J.* **9**, 332–341 (2003).
- Ponath, G. et al. Myelin phagocytosis by astrocytes after myelin damage promotes lesion pathology. *Brain* **140**, 399–413 (2017).
- Ruckh, J. M. et al. Rejuvenation of regeneration in the aging central nervous system. *Cell Stem Cell* **10**, 96–103 (2012).
- Yuste-Checa, P., Bracher, A. & Hartl, F. U. The chaperone clusterin in neurodegeneration—friend or foe? *Bioessays* **44**, e2100287 (2022).
- Cordero-Llana, O. et al. Clusterin secreted by astrocytes enhances neuronal differentiation from human neural precursor cells. *Cell Death Differ.* **18**, 907–913 (2011).
- Stoop, M. P. et al. Multiple sclerosis-related proteins identified in cerebrospinal fluid by advanced mass spectrometry. *Proteomics* **8**, 1576–1585 (2008).
- Kroksveen, A. C. et al. Discovery and initial verification of differentially abundant proteins between multiple sclerosis patients and controls using iTRAQ and SID-SRM. *J. Proteom.* **78**, 312–325 (2013).
- Stoop, M. P. et al. Quantitative matrix-assisted laser desorption/ionization-Fourier transform ion cyclotron resonance (MALDI-FT-ICR) peptide profiling and identification of multiple-sclerosis-related proteins. *J. Proteome Res.* **8**, 1404–1414 (2009).
- Fiorini, A. et al. Involvement of oxidative stress in occurrence of relapses in multiple sclerosis: the spectrum of oxidatively modified serum proteins detected by proteomics and redox proteomics analysis. *PLoS ONE* **8**, e65184 (2013).
- Rithidech, K. N. et al. Protein expression profiles in pediatric multiple sclerosis: potential biomarkers. *Mult. Scler. J.* **15**, 455–464 (2009).
- Razia, R. et al. The analysis of dynamic gene expression patterns in peripheral blood of multiple sclerosis patients indicates possible diagnostic and prognostic biomarkers. *Mol. Immunol.* **147**, 147–156 (2022).
- Polihronis, M., Paizis, K., Carter, G., Sedal, L. & Murphy, B. Elevation of human cerebrospinal fluid clusterin concentration is associated with acute neuropathology. *J. Neurol. Sci.* **115**, 230–233 (1993).
- Ingram, G. et al. Complement activation in multiple sclerosis plaques: an immunohistochemical analysis. *Acta Neuropathol. Commun.* **2**, 53 (2014).
- Loveless, S. et al. Tissue microarray methodology identifies complement pathway activation and dysregulation in progressive multiple sclerosis. *Brain Pathol.* **28**, 507–520 (2018).
- Zhou, Y. et al. Metascape provides a biologist-oriented resource for the analysis of systems-level datasets. *Nat. Commun.* **10**, 1523 (2019).
- Wan, T. et al. Astrocytic phagocytosis contributes to demyelination after focal cortical ischemia in mice. *Nat. Commun.* **13**, 1134 (2022).
- Langley, M. R. et al. Critical role of astrocyte NAD⁺ glycohydrolase in myelin injury and regeneration. *J. Neurosci.* **41**, 8644–8667 (2021).
- Sen, M. K., Mahns, D. A., Coorsen, J. R. & Shortland, P. J. The roles of microglia and astrocytes in phagocytosis and myelination: insights from the cuprizone model of multiple sclerosis. *Glia* **70**, 1215–1250 (2022).
- Leeb, C., Eresheim, C. & Nimpf, J. Clusterin is a ligand for apolipoprotein E receptor 2 (ApoER2) and very low density lipoprotein receptor (VLDLR) and signals via the Reelin-signaling pathway. *J. Biol. Chem.* **289**, 4161–4172 (2014).
- Riaz, M. A., Stammer, A., Borgers, M. & Konrad, L. Clusterin signals via ApoER2/VLDLR and induces meiosis of male germ cells. *Am. J. Transl. Res.* **9**, 1266–1276 (2017).
- Dlugosz, P. & Nimpf, J. The Reelin receptors apolipoprotein E receptor 2 (ApoER2) and VLDL receptor. *Int. J. Mol. Sci.* **19**, 3090 (2018).
- Cuitino, L. et al. ApoER2 is endocytosed by a clathrin-mediated process involving the adaptor protein Dab2 independent of its Rafts' association. *Traffic* **6**, 820–838 (2005).

34. Herring, S. K., Moon, H. J., Rawal, P., Chhibber, A. & Zhao, L. Brain clusterin protein isoforms and mitochondrial localization. *Elife* **8**, e48255 (2019).
35. Lambert, J. C. et al. Genome-wide association study identifies variants at CLU and CR1 associated with Alzheimer's disease. *Nat. Genet.* **41**, 1094–1099 (2009).
36. Harold, D. et al. Genome-wide association study identifies variants at CLU and PICALM associated with Alzheimer's disease. *Nat. Genet.* **41**, 1088–1093 (2009).
37. Wojtas, A. M. et al. Astrocyte-derived clusterin suppresses amyloid formation in vivo. *Mol. Neurodegener.* **15**, 71 (2020).
38. Liu, X. et al. Clusterin transduces Alzheimer-risk signals to amyloidogenesis. *Signal Transduct. Target. Ther.* **7**, 325 (2022).
39. Wojtas, A. M. et al. Loss of clusterin shifts amyloid deposition to the cerebrovasculature via disruption of perivascular drainage pathways. *Proc. Natl Acad. Sci. USA* **114**, E6962–E6971 (2017).
40. Foster, E. M., Dangla-Valls, A., Lovestone, S., Ribe, E. M. & Buckley, N. J. Clusterin in Alzheimer's disease: mechanisms, genetics, and lessons from other pathologies. *Front. Neurosci.* **13**, 164 (2019).
41. Chen, F. et al. Clusterin secreted from astrocyte promotes excitatory synaptic transmission and ameliorates Alzheimer's disease neuropathology. *Mol. Neurodegener.* **16**, 5 (2021).
42. Killick, R. et al. Clusterin regulates beta-amyloid toxicity via Dickkopf-1-driven induction of the wnt-PCP-JNK pathway. *Mol. Psychiatr.* **19**, 88–98 (2014).
43. Robbins, J. P. et al. Clusterin is required for β -amyloid toxicity in human iPSC-derived neurons. *Front. Neurosci.* **12**, 504 (2018).
44. Liu, Z. et al. Astrocytic response mediated by the CLU risk allele inhibits OPC proliferation and myelination in a human iPSC model. *Cell Rep.* **42**, 112841 (2023).
45. Braskie, M. N. et al. Common Alzheimer's disease risk variant within the CLU gene affects white matter microstructure in young adults. *J. Neurosci.* **31**, 6764–6770 (2011).
46. Konishi, H. et al. Astrocytic phagocytosis is a compensatory mechanism for microglial dysfunction. *EMBO J.* **39**, e104464 (2020).
47. Wang, S. et al. Astrocytes directly clear myelin debris through endocytosis pathways and followed by excessive gliosis after spinal cord injury. *Biochem. Biophys. Res. Commun.* **525**, 20–26 (2020).
48. Gaultier, A. et al. Low-density lipoprotein receptor-related protein 1 is an essential receptor for myelin phagocytosis. *J. Cell Sci.* **122**, 1155–1162 (2009).
49. Tian, Y. et al. Extracellular Hsp90 α and clusterin synergistically promote breast cancer epithelial-to-mesenchymal transition and metastasis via LRP1. *J. Cell Sci.* **132**, jcs228213 (2019).
50. Bell, R. D. et al. Transport pathways for clearance of human Alzheimer's amyloid beta-peptide and apolipoproteins E and J in the mouse central nervous system. *J. Cereb. Blood Flow. Metab.* **27**, 909–918 (2007).
51. Baralla, A. et al. Plasma clusterin and lipid profile: a link with aging and cardiovascular diseases in a population with a consistent number of centenarians. *PLoS ONE* **10**, e128029 (2015).
52. Heo, J. Y. et al. Clusterin deficiency induces lipid accumulation and tissue damage in kidney. *J. Endocrinol.* **237**, 175–191 (2018).
53. Hammel, G., Zivkovic, S., Ayazi, M. & Ren, Y. Consequences and mechanisms of myelin debris uptake and processing by cells in the central nervous system. *Cell. Immunol.* **380**, 104591 (2022).
54. Gil, S. Y. et al. Clusterin and LRP2 are critical components of the hypothalamic feeding regulatory pathway. *Nat. Commun.* **4**, 1862 (2013).
55. Wilson, M. R. & Easterbrook-Smith, S. B. Clusterin is a secreted mammalian chaperone. *Trends Biochem. Sci.* **25**, 95–98 (2000).
56. Yerbury, J. J. et al. The extracellular chaperone clusterin influences amyloid formation and toxicity by interacting with prefibrillar structures. *FASEB J.* **21**, 2312–2322 (2007).
57. Philips, T. & Rothstein, J. D. Oligodendroglia: metabolic supporters of neurons. *J. Clin. Invest.* **127**, 3271–3280 (2017).
58. Mishra, M. K. et al. Harnessing the benefits of neuroinflammation: generation of macrophages/microglia with prominent remyelinating properties. *J. Neurosci.* **41**, 3366–3385 (2021).
59. Lubetzki, C., Zalc, B., Williams, A., Stadelmann, C. & Stankoff, B. Remyelination in multiple sclerosis: from basic science to clinical translation. *Lancet Neurol.* **19**, 678–688 (2020).
60. Franklin, R., Frisen, J. & Lyons, D. A. Revisiting remyelination: towards a consensus on the regeneration of CNS myelin. *Semin. Cell Dev. Biol.* **116**, 3–9 (2021).
61. Kuhlmann, T. et al. Differentiation block of oligodendroglial progenitor cells as a cause for remyelination failure in chronic multiple sclerosis. *Brain* **131**, 1749–1758 (2008).
62. Zirngibl, M., Assinck, P., Sizov, A., Capriarello, A. V. & Plemel, J. R. Oligodendrocyte death and myelin loss in the cuprizone model: an updated overview of the intrinsic and extrinsic causes of cuprizone demyelination. *Mol. Neurodegener.* **17**, 34 (2022).
63. Kipp, M. Astrocytes: lessons learned from the cuprizone model. *Int. J. Mol. Sci.* **24**, 16420 (2023).
64. Chen, J. F. et al. Enhancing myelin renewal reverses cognitive dysfunction in a murine model of Alzheimer's disease. *Neuron* **109**, 2292–2307 (2021).
65. Haileselassie, B. et al. Mitochondrial dysfunction mediated through dynamin-related protein 1 (Drp1) propagates impairment in blood brain barrier in septic encephalopathy. *J. Neuroinflamm.* **17**, 36 (2020).
66. Lee, J. Y. et al. Neuronal SphK1 acetylates COX2 and contributes to pathogenesis in a model of Alzheimer's Disease. *Nat. Commun.* **9**, 1479 (2018).
67. Lee, J. Y. et al. N-AS-triggered SPMs are direct regulators of microglia in a model of Alzheimer's disease. *Nat. Commun.* **11**, 2358 (2020).

Acknowledgements

We acknowledge Professor Ke Li of the Guangdong Laboratory Animals Monitoring Institute for providing us with the Aldh1l1-CreERT mice. We also acknowledge Professor Bo Peng of the Fudan University for providing guidance on this subject, and Professor Xiaoyan Han for offering equipment support. Q.W. gratefully acknowledges funding by the National Natural Science Foundation of China (81971140, 82271377), Key project of Guangdong Basic and Applied Basic Research Fund (2022B1515120042) and Municipal Key Laboratory Construction Project (202102010009). S.Y.Q. gratefully acknowledges funding by the Natural Science Foundation of China (82071343, 82371354, 81701188), the Guangdong Basic and Applied Basic Research Fund (2021A1515010393) and Guangzhou Municipal School (Hospital) Joint Funding (202201020415).

Author contributions

All authors have contributed significantly to this work. C.C., Y.Q.S., C.K.Y., X.D.L., F.M., F.Q. and W.Q. conceived and designed the experiments; C.C., Y.Q.S., and C.K.Y. performed the majority of the experiments; Y.Q.S., C.K.Y., H.L.L., Z.C.H., Y.J.J., S.X.H., Z.H.W., and F.Q. contributed to data collection and provided experimental support; C.C., Y.Q.S., X.D.L., H.L.L., Z.C.H., C.X.L., S.S.S., Z.C.H., and W.Q. analyzed and interpreted the data; C.C., Y.Q.S., and X.D.L. wrote the manuscript; C.C., Y.Q.S., X.D.L., and W.Q. revised and edited the manuscript. All authors read and approved the final manuscript.

Competing interests

The authors declare no competing interests.

Additional information

Supplementary information The online version contains supplementary material available at <https://doi.org/10.1038/s41467-024-52142-7>.

Correspondence and requests for materials should be addressed to Feng Qin, Xiaodong Liu or Wei Qiu.

Peer review information *Nature Communications* thanks Vittorio Gallo and the other anonymous reviewer(s) for their contribution to the peer review of this work. A peer review file is available.

Reprints and permissions information is available at <http://www.nature.com/reprints>

Publisher's note Springer Nature remains neutral with regard to jurisdictional claims in published maps and institutional affiliations.

Open Access This article is licensed under a Creative Commons Attribution-NonCommercial-NoDerivatives 4.0 International License, which permits any non-commercial use, sharing, distribution and reproduction in any medium or format, as long as you give appropriate credit to the original author(s) and the source, provide a link to the Creative Commons licence, and indicate if you modified the licensed material. You do not have permission under this licence to share adapted material derived from this article or parts of it. The images or other third party material in this article are included in the article's Creative Commons licence, unless indicated otherwise in a credit line to the material. If material is not included in the article's Creative Commons licence and your intended use is not permitted by statutory regulation or exceeds the permitted use, you will need to obtain permission directly from the copyright holder. To view a copy of this licence, visit <http://creativecommons.org/licenses/by-nc-nd/4.0/>.

© The Author(s) 2024